Geochemical Perspectives Letters

Oxygenation of the mid-Proterozoic atmosphere: clues from chromium isotopes in carbonates

G.J. Gilleaudeau[1,2*], R. Frei[1], A.J. Kaufman[3], L.C. Kah[4], K. Azmy[5], J.K. Bartley[6], P. Chernyavskiy[7], A.H. Knoll[8]

OPEN ACCESS

Abstract

doi: 10.7185/geochemlet.1618

Chromium (Cr) isotopes in marine sedimentary rocks can be used as a sensitive proxy for ancient atmospheric oxygen because Cr-isotope fractionation during terrestrial weathering only occurs when pO_2 exceeds a threshold value. This is a useful system when applied to rocks of mid-Proterozoic age, where fundamental questions persist about atmospheric pO_2 and its relationship to biological innovation. Whereas previous studies have focused on temporally limited iron-rich sedimentary rocks, we present new Cr-isotope data from a suite of mid-Proterozoic marine carbonate rocks. Application of the Cr-isotope proxy to carbonate rocks has the potential to greatly enhance the temporal resolution of Proterozoic palaeoredox data. Here we report positive $\delta^{53}Cr$ values in four carbonate successions, extending the mid-Proterozoic record of Cr-isotope fractionation – and thus pO_2 above threshold values – back to ~1.1 Ga. These data suggest that pO_2 sufficient for the origin of animals was transiently in place well before their Neoproterozoic appearance, although uncertainty in the pO_2 threshold required for Cr-isotope fractionation precludes definitive biological interpretation. This study provides a proof of concept that the Cr-isotopic composition of carbonate rocks can provide important new constraints on the oxygen content of the ancient atmosphere.

Received 11 March 2015 | Accepted 9 May 2016 | Published 24 May 2016

1. Department of Geosciences and Natural Resource Management, University of Copenhagen, Øster Voldgade 10, 1350 Copenhagen, Denmark
2. Current address: School of Earth and Space Exploration, Arizona State University, Tempe, AZ 85281, USA
* Corresponding author: (email: ggillea1@gmail.com)
3. Department of Geology, University of Maryland, College Park, MD 20742, USA
4. Department of Earth and Planetary Sciences, University of Tennessee, Knoxville, TN 37996, USA
5. Department of Earth Sciences, Memorial University of Newfoundland, St. John's, Newfoundland A1B 3X5, Canada
6. Department of Geology, Gustavus Adolphus College, St. Peter, MN 56082, USA
7. Biostatistics/Radiation Epidemiology Branch, National Cancer Institute, National Institutes of Health, Rockville, MD 20850, USA
8. Department of Organismic and Evolutionary Biology, Harvard University, Cambridge, MA 02138, USA

Introduction

The chromium (Cr) isotope system functions as an atmospheric redox proxy because oxidative weathering of crustal Cr(III)-bearing minerals results in the release of ^{53}Cr-enriched mobile Cr(VI) to solution. Cr(VI) (dominantly as chromate; CrO_4^-) is then carried to the oceans via rivers, thus imparting a positively fractionated $\delta^{53}Cr$ signal on modern seawater (+0.41 to +1.55 ‰ compared to crustal values of –0.123 ± 0.102 ‰) (Schoenberg *et al.*, 2008; Bonnand *et al.*, 2013; Scheiderich *et al.*, 2015). Terrestrial Cr(III)-oxidation occurs by reaction with manganese (Mn) oxides, and it is thought that Mn-oxide formation requires a threshold level of O_2 in the atmosphere. Frei *et al.* (2016) suggested that Cr-oxidation by Mn-oxides is thermodynamically possible at pO_2 as low as 10^{-5} of the present atmospheric level (PAL). Kinetic considerations dictate, however, that 0.1 to 1 % PAL is necessary to oxidise Cr(III) within typical soil residence times (Planavsky *et al.*, 2014) and between 0.03 and 0.3 % PAL is necessary to export Cr without re-reduction by Fe(II) (Crowe *et al.*, 2013). Because the delivery of positively fractionated Cr(VI) to seawater is dependent on a threshold level of atmospheric oxygen, the Cr-isotope composition of seawater through time – as recorded in marine sedimentary rocks – can serve as a sensitive indicator of ancient atmospheric pO_2. This is particularly useful for testing hypotheses about atmospheric oxygenation during the Proterozoic Eon, where fundamental questions persist about the O_2 content of Earth's atmosphere and its relationship to temporal patterns of biological innovation.

The oxygenation of Earth surface environments was a protracted process that occurred over >2 billion years (Ga) (see Lyons *et al.*, 2014). Two first-order oxygen pulses have been identified from the Proterozoic geologic record. During the Great Oxidation Event (GOE) at ~2.4 Ga, pO_2 was sustained above 10^{-5} PAL for the first time in Earth history, although transient 'whiffs' of O_2 have been recognised from the Archaean geochemical record. During a subsequent Neoproterozoic oxygenation event (NOE) at ~635-550 Ma, pO_2 began to rise to near-modern levels – a transition that continued into the Palaeozoic Era.

Empirical constraints remain limited, however, on pO_2 during the prolonged period in between. Constraining pO_2 during the mid-Proterozoic Eon has major implications for understanding potential biogeochemical controls on the timing of animal diversification. Some argue that exceedingly low mid-Proterozoic pO_2 was a direct impediment to metazoan evolution prior to the Neoproterozoic Era (Planavsky *et al.*, 2014), whereas others argue that oxygen levels required by early animals were in place long before their Neoproterozoic appearance (Butterfield, 2009; Zhang *et al.*, 2016). Mid-Proterozoic Cr-isotope data have the potential to inform this debate because estimates of the pO_2 threshold needed for Cr-isotope fractionation are roughly similar to experimental and theoretical estimates of the O_2 requirements of early animals (0.3 to 4 % PAL) (*e.g.*, Mills *et al.*, 2014).

Thus far, studies have largely focused on iron-rich sedimentary rocks as an archive for ancient seawater $\delta^{53}Cr$ values. In the presence of Fe(II), seawater Cr(VI) is reduced to Cr(III) and can be co-precipitated with Fe-(oxyhydr)oxides. Cr-reduction favours the light ^{52}Cr isotope, so that iron-rich rocks record seawater $\delta^{53}Cr$ values only if Cr-reduction is quantitative. Ironstone and iron formation data have thus far provided important constraints on Archaean 'whiffs' of oxygen and the subsequent GOE, as well as new clues about the NOE (Frei *et al.*, 2009). Sparse ironstone data from the mid-Proterozoic suggest a lack of Cr-isotope fractionation (Planavsky *et al.*, 2014). Iron-rich rocks are rare in mid-Proterozoic successions, however, limiting our ability to generate data for the crucial period preceding the NOE.

The impetus of this study, then, is to test the reliability of Cr-isotopes in marine carbonate rocks that are ubiquitous in the mid-Proterozoic geologic record. A potential advantage of using carbonate rocks as a Cr-isotope archive is that chromate can be incorporated into the lattice of carbonate minerals with no change in oxidation state. Studies of modern invertebrate shells reveal that Cr-isotope fractionation does occur during biomineralisation, making skeletal carbonates an unreliable archive of seawater $\delta^{53}Cr$ values (Pereira *et al.*, 2016). Mohanta *et al.* (2016) showed that modern bulk biogenic carbonate is as much as 0.45 ‰ lighter than seawater. Co-precipitation experiments involving chromate incorporation into calcite have shown, however, that abiogenic carbonate has the potential to record $\delta^{53}Cr$ values of the ambient solution (Rodler *et al.*, 2015). In experiments with the lowest initial Cr concentration (8.6 ppm), precipitates were <0.1 ‰ heavier than the solution, suggesting that minimal fractionation occurs during chromate incorporation into calcite at low Cr concentrations typical of seawater (0.08 to 0.5 ppm).

In this study, we measured the Cr-isotopic composition of marine limestone and dolostone from four geographically distinct mid-Proterozoic successions, along with a suite of major and trace elements to constrain diagenetic pathways and the influence of detrital contamination. We focused on the interval between ~1.1 and 0.9 Ga – where sea level highstand resulted in marine carbonate deposition across multiple cratons – and a variety of depositional environments to assess the consistency and reliability of the proxy. Samples were carefully selected based on known criteria for identifying diagenetic alteration and detrital contamination, and our data are ultimately used to provide important new constraints on atmospheric pO_2 during the mid-Proterozoic Eon.

Background and Methods

Samples were analysed from the Turukhansk Uplift, Siberia (~900-1035 Ma), the Angmaat Formation, Canada (~1092 Ma), the El Mreiti Group, Mauritania (~1107 Ma), and the Vazante Group, Brazil (~1112 Ma). Cr-isotope and Cr concentration measurements were performed on a thermal ionisation mass spectrometer. Ca, Mg, Fe, Sr, Mn, and Al concentrations were measured by ICP-OES, and Ti and Zr concentrations were measured by ICP-MS (see Supplementary Information).

Diagenesis

The chemical reactivity of carbonate minerals during diagenesis requires detailed understanding of potential diagenetic processes prior to selecting samples for Cr-isotope analysis. Here we employ a robust set of screening criteria for sample inclusion. Conventional light and cathodoluminescence petrography permit recognition of recrystallisation processes and secondary phases, and a combination of isotopic and elemental analyses provide evidence for fluid alteration based on the relative mobility of ions within lattice components. In short, samples containing substantial evidence for diagenetic alteration (*e.g.*, Ostwald ripening, loss of fabric details, and secondary precipitation phases) were excluded (Figs. S-1, S-2). We then compared isotopic and trace element trends that are sensitive to fluid interaction (*e.g.*, $\delta^{18}O$, [Sr], [Mn]; Banner and Hanson, 1990) to values recorded across a range of preservation states within Proterozoic carbonates (*e.g.*, Kaufman and Knoll, 1995; Bartley *et al.*, 2007; Kah *et al.*, 2012), conservatively excluding outliers that are depleted in ^{18}O, substantially enriched in Mn, or depleted in Sr (Fig. S-3). We interpret our Cr-isotope data within the context of these standard criteria, acknowledging that additional work is necessary specifically to explore Cr behaviour during carbonate diagenesis. Detailed mineralogical, textural, and geochemical information can be found in the Supplementary Information.

Detrital Chromium

Our results indicate a broad range of $\delta^{53}Cr$ values in each succession, ranging from crustal values (near –0.12 ‰) to strongly positive values (up to +1.77 ‰). To understand this isotopic heterogeneity, we first evaluated the degree to which measured $\delta^{53}Cr$ values reflect authigenic Cr in carbonate vs. allogenic Cr from detrital sources. As part of each dissolution for $\delta^{53}Cr$ analysis, we measured a split for aluminium (Al) content to assess the degree to which clay – which can be a host phase for detrital Cr – was leached during dissolution. In a plot of Al concentration in the leachate *vs.* raw $\delta^{53}Cr$ values (Fig. 1a), positively fractionated $\delta^{53}Cr$ is only recorded in samples where less than ~400 ppm Al is leached. A similar trend is observed for other detrital indicators. Positively fractionated $\delta^{53}Cr$ is only observed when leachate titanium (Ti) and zirconium (Zr) concentrations are generally less than 10 and 1 ppm, respectively (Fig. S-4), although the relationship is not well-defined for Zr. Assuming that Al is the most effective indicator of clay contamination, we compared sample Cr/Al ratios to an average shale composite (Cr = 90 ppm; Al = 8.89 wt. %; Wedepohl, 1991) – which serves as a first-order proxy for clay-rich detrital sediment – to derive a rough estimate of the fraction of Cr sourced from detrital material for each sample. Similarly, positively fractionated $\delta^{53}Cr$ is only recorded in samples where less than ~35 % of measured Cr is detritally sourced (Fig. 1b).

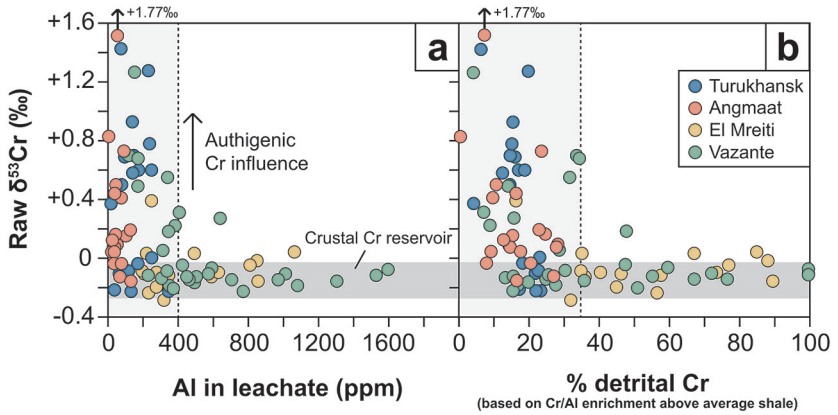

Figure 1 **(a)** Cross-plot of raw Cr-isotope values and Al concentration in the leachate. Dashed line is at 400 ppm Al. **(b)** Cross-plot of raw Cr-isotope values and % detrital Cr based on enrichment above average shale. Dashed line is at 35 %.

These trends represent a mixing curve where Cr in the carbonate lattice is dissolved and analysed in addition to Cr leached from clay. When detrital Cr exceeds ~35 % of total measured Cr, δ^{53}Cr values approach average crust (–0.12 ‰) and the isotopic composition of the authigenic seawater component is unresolvable. When samples have less than ~35 % detrital Cr, we can perform a basic correction of raw δ^{53}Cr values, assuming the detrital component has a crustal δ^{53}Cr value. This yields a first-order estimate of the isotopic composition of the authigenic Cr component ($\delta^{53}Cr_{auth}$), which is thought to be derived from seawater (see Supplementary Information).

After exclusion of samples based on diagenetic and detrital contamination criteria, our dataset consisted of 62 samples that cover all four successions. These methods for assessing detrital Cr contamination represent a new set of best practices that should be applied in future Cr-isotope studies of carbonate rocks.

Atmospheric Oxygen

The main observation of our dataset is that all four successions record positively fractionated $\delta^{53}Cr_{auth}$ values. The maximum isotopic difference observed by Rodler *et al.* (2015) between synthetic calcite and ambient solution was 0.33 ‰ so that, even if some fractionation did occur during carbonate formation, the preponderance of strongly positive δ^{53}Cr values in our dataset (n = 24 samples >0.3 ‰) indicates that mid-Proterozoic seawater was positively fractionated. Additionally, if carbonate preferentially incorporated ^{52}Cr as observed by Mohanta *et al.* (2016), then our dataset provides even stronger evidence for positively fractionated Cr in mid-Proterozoic seawater, assuming that carbonates are able to retain their original δ^{53}Cr signature.

The record of positively fractionated Cr in seawater has recently been extended back to ~3.8 Ga, which Frei *et al.* (2016) interpret as terrestrial Cr-oxidation under an otherwise anoxic Archaean atmosphere. Banded iron formations from the Archaean-Proterozoic transition record pulses of terrestrial Cr-oxidation prior to the GOE and a lack of Cr-isotope fractionation immediately following the GOE, which is interpreted as a post-GOE decline in atmospheric pO_2 (Frei *et al.*, 2009). Subsequent evidence for Cr-isotope fractionation was not found until ~750 Ma (Planavsky *et al.*, 2014), leading to the suggestion that low pO_2 inhibited Cr-isotope fractionation during the mid-Proterozoic Eon. Here we extend the mid-Proterozoic record of positively fractionated Cr back to ~1.1 Ga – a revision of ~350 Ma from previous estimates (Fig. 2).

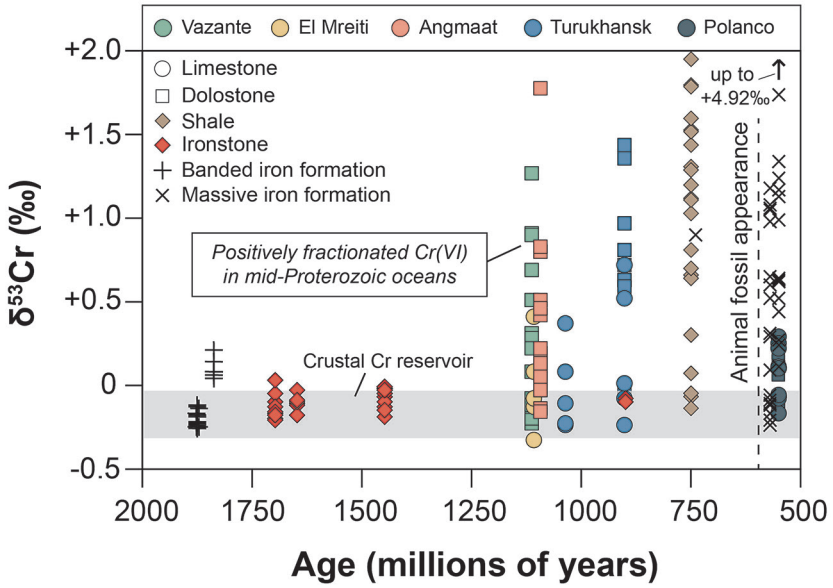

Figure 2 Compilation of all published Proterozoic Cr-isotope data including new data presented here. $\delta^{53}Cr_{auth}$ values (after detrital correction) are presented for data from this study.

At present, there is no clear consensus on the pO_2 level required for Cr-isotope fractionation during terrestrial weathering. If we take soil residence time calculations (~0.1 to 1 % PAL; Planavsky *et al.*, 2014) as our best estimate, we conclude that pO_2 at least transiently exceeded ~0.1 to 1 % PAL during the mid-Proterozoic Eon. These data are consistent with a broad range of proxies that suggest increasing biospheric oxygen in the Mesoproterozoic Era (Kah *et al.*, 2001; Johnston *et al.*, 2005; Parnell *et al.*, 2010; Zhang *et al.*, 2016). Data are potentially inconsistent, however, with recent estimates of maximum pO_2 between 0.1 and 1 % PAL during the mid-Proterozoic Eon, including Cr-isotope data from sparse mid-Proterozoic iron oolites (Planavsky *et al.*, 2014; Liu *et al.*, 2016).

Potential conflict between our data and other proxies could be related to uncertainty regarding the pO_2 threshold required for Cr-isotope fractionation. If we take 0.03 % PAL as the required threshold, for example, our data become compatible with the pO_2 estimate of Liu *et al.* (2016) based on carbonate Zn/Fe systematics. Regardless of the threshold value, however, our data remain inconsistent with Cr-isotope data from mid-Proterozoic iron oolites. This discrepancy cannot be explained by Cr-isotope fractionation during carbonate formation, particularly if carbonates preferentially incorporate ^{52}Cr (Mohanta *et al.*, 2016), which would only amplify evidence for positively fractionated Cr in mid-Proterozoic seawater. We have also robustly screened our samples for diagenesis using standard petrographic and geochemical criteria, although diagenetic effects cannot be completely discounted given uncertainty regarding Cr behaviour during carbonate diagenesis. To this end, we compared $\delta^{53}Cr$ to $\delta^{18}O$ as a diagenetic indicator, and found that the lowest $\delta^{18}O$ values in our dataset – normally thought to reflect diagenetic alteration – are associated with unfractionated $\delta^{53}Cr$ values (Fig. S-5). This could indicate that, at least in our dataset, diagenesis is more likely to give a false negative than a false positive result. Another possibility is that ironstone data do not record seawater $\delta^{53}Cr$ because of partial Cr-reduction during precipitation of shallow water iron oolites, which may have occurred under fluctuating redox conditions. As articulated by Planavsky *et al.* (2014), however, this would be expected to generate a range of $\delta^{53}Cr$ values – not the persistently unfractionated values that were measured.

Another alternative is that mid-Proterozoic pO_2 was variable around the threshold required for Cr-isotope fractionation. There is evidence for this in our dataset – the persistence of unfractionated $\delta^{53}Cr$ values that are not related to detrital contamination (Fig. 1) could be related to transient periods of pO_2 below threshold values. Indeed the only measured iron oolites that temporally overlap with samples from this study are limited samples from the ~0.9 Ga Aok Formation (Canada), implying that the coarse temporal resolution of current data may be insufficient to track short-term variability in pO_2. Taken together with the full range of published proxy data, we conclude that mid-Proterozoic pO_2 was likely more dynamic than previously envisaged.

Biological Implications

Implications of our data on biospheric evolution are similarly tied to uncertainty regarding the pO_2 threshold needed for Cr-isotope fractionation. Tank experiments have shown that sponges can survive when pO_2 is as low as 0.5 to 4 % PAL, leading Mills *et al.* (2014) to conclude that this level was likely sufficient for the origin of animals. Based on theoretical early annelid body plans, a small worm with a circulatory system could likely survive at pO_2 as low as 0.14 % PAL (Sperling *et al.*, 2013a). Studies from modern oxygen minimum zones confirm these estimates and suggest that the bilaterian body plan would only be inhibited if pO_2 were below 0.4 % PAL. If we take 0.1 to 1 % PAL as the threshold required for Cr-isotope fractionation, then our data suggest that pO_2 levels sufficient for the origin of animals were at least transiently in place by ~1.1 Ga – some 300 Ma before the origin of sponges based on molecular clock estimates (Erwin *et al.*, 2011) and >450 Ma before the first appearance of animals in the fossil record. By contrast, if we take a lower threshold value of 0.03 % PAL, then our data have less direct implications for biology. Ecological considerations are also important and modern oxygen minimum zones suggest that there is a clear linkage between oxygen availability, animal size, and the relative proportion of carnivorous taxa (Sperling *et al.*, 2013b). Based on these considerations it seems that, although the oxygen requirements of small, simple animals were likely met by ~1.1 Ga, low atmospheric pO_2 may still have inhibited the development of larger, more energetic animals that have greater preservation potential in the fossil record.

Conclusions

This study demonstrates the viability of the Cr-isotope palaeo-redox proxy as it is applied to ancient carbonate rocks. After screening for detrital contamination – and assuming that our least-altered samples are able to retain original $\delta^{53}Cr$ values – Cr-isotope data can be interpreted in the context of ancient atmospheric pO_2. Results from four carbonate successions extend the mid-Proterozoic record of positively fractionated Cr back to ~1.1 Ga – a revision of ~350 Ma from previous estimates. If we take 0.1 to 1 % PAL as the pO_2 threshold needed for Cr-isotope fractionation, then our data suggest that the oxygen requirements of small, simple animals were at least transiently met well prior to their Neoproterozoic appearance, although uncertainty regarding this pO_2 threshold precludes definitive biological interpretation. Ultimately, the development of novel carbonate-based redox proxies has the potential to greatly enhance the temporal resolution of palaeo-redox data for the Proterozoic Eon.

Acknowledgements

This work was supported by grants from the Danish Natural Science Research Council (FNU) to R.F. and the Carlsberg Foundation to G.J.G. and R.F. A.H.K. thanks the NASA Astrobiology Institute and G.J.G. thanks Ariel Anbar and the NASA Postdoctoral Program. We are indebted to Toni Larsen for help in ion chromatographic separation of Cr, Toby Leeper for mass spectrometry support, Jørgen Kystol for running the ICP-MS, and Andrea Voegelin for major contributions to Cr-isotope analytical and data interpretation techniques. We also thank Clemens V. Ullmann for ICP-OES expertise and insightful comments on an earlier draft of this manuscript.

Editor: Eric H. Oelkers

Additional Information

Supplementary Information accompanies this letter at www.geochemicalperspectivesletters.org/article1618

Reprints and permission information is available online at http://www.geochemicalperspectivesletters.org/copyright-and-permissions

Cite this letter as: Gilleaudeau, G.J., Frei, R., Kaufman, A.J., Kah, L.C., Azmy, K., Bartley, J.K., Chernyavskiy, P., Knoll, A.H. (2016) Oxygenation of the mid-Proterozoic atmosphere: clues from chromium isotopes in carbonates. *Geochem. Persp. Let.* 2, 178-187.

References

Banner, J.L., Hanson, G.N. (1990) Calculation of simultaneous isotopic and trace element variations during water-rock interaction with applications to carbonate diagenesis. *Geochimica et Cosmochimica Acta* 54, 3123-3137.

Bartley, J.K., Kah, L.C., McWilliams, J.L., Stagner, A.F. (2007) Carbon isotope chemostratigraphy of the Middle Riphean type section (Avzyan Formation, Southern Urals, Russia): signal recovery in a fold-and-thrust belt. *Chemical Geology* 237, 211-232.

Bonnand, P., James, R.H., Parkinson, I.J., Connelly, D.P., Fairchild, I.J. (2013) The chromium isotopic composition of seawater and marine carbonates. *Earth and Planetary Science Letters* 382, 10-20.

Butterfield, N.J. (2009) Oxygen, animals and oceanic ventilation: an alternative view. *Geobiology* 7, 1-7.

Crowe, S.A., Døssing, L.N., Beukes, N.J., Bau, M., Kruger, S.J., Frei, R., Canfield, D.E. (2013) Atmospheric oxygenation three billion years ago. *Nature* 501, 535-538.

Erwin, D.H., Laflamme, M., Tweedt, S.M., Sperling, E.A., Pisani, D., Peterson, K.J. (2011) The Cambrian conundrum: early divergence and later ecological success in the early history of animals. *Science* 334, 1091-1097.

Frei, R., Gaucher, C., Poulton, S.W., Canfield, D.E. (2009) Fluctuations in Precambrian atmospheric oxygenation recorded by chromium isotopes. *Nature* 461, 250-253.

Frei, R., Crowe, S.A., Bau, M., Polat, A., Fowle, D.A., Døssing, L.N. (2016) Oxidative elemental cycling under the low O_2 Eoarchean atmosphere. *Scientific Reports* 6, 21058.

Johnston, D.T., Wing, B.A., Farquhar, J., Kaufman, A.J., Strauss, H., Lyons, T.W., Kah, L.C., Canfield, D.E. (2005) Active microbial sulfur disproportionation in the Mesoproterozoic. *Science* 310, 1477-1479.

Kah, L.C., Lyons, T.W., Chesley, J.T. (2001) Geochemistry of a 1.2 Ga carbonate-evaporite succession, northern Baffin and Bylot Islands: implications for Mesoproterozoic marine evolution. *Precambrian Research* 111, 203-234.

Kah, L.C., Bartley, J.K., Teal, D.A. (2012) Chemostratigraphy of the late Mesoproterozoic Atar Group, Taoudeni Basin, Mauritania: muted isotopic variability, facies correlation, and global isotopic trends. *Precambrian Research* 200-203, 82-103.

Kaufman, A.J., Knoll, A.H. (1995) Neoproterozoic variations in the C-isotopic composition of seawater: stratigraphic and biogeochemical implications. *Precambrian Research* 73, 27-49.

Liu, X.M., Kah, L.C., Knoll, A.H., Cui, H., Kaufman, A.J., Shahar, A., Hazen, R.M. (2016) Tracing Earth's O_2 evolution using Zn/Fe ratios in marine carbonates. *Geochemical Perspectives Letters* 2, 24-34.

Lyons, T.W., Reinhard, C.T., Planavsky, N.J. (2014) The rise of oxygen in Earth's early ocean and atmosphere. *Nature* 506, 307-315.

Mills, D.B., Ward, L.M., Jones, C., Sweeten, B., Forth, M., Treusch, A.H., Canfield, D.E. (2014) Oxygen requirements of the earliest animals. *Proceedings of the National Academy of Sciences USA* 111, 4168-4172.

Mohanta, J., Holmden, C., Blanchon, P. (2016) Chromium isotope fractionation between seawater and carbonate sediment in the Caribbean Sea. *Goldschmidt Abstracts*, http://goldschmidt.info/2016/uploads/abstracts/finalPDFs/2121.pdf.

Parnell, J., Boyce, A.J., Mark, D., Bowden, S., Spinks, S. (2010) Early oxygenation of the terrestrial environment during the Mesoproterozoic. *Nature* 468, 290-293.

Pereira, N.S., Voegelin, A.R., Paulukat, C., Sial, A.N., Ferreira, V.P., Frei, R. (2016) Chromium-isotope signatures in scleractinian corals from the Rocas Atoll, Tropical South Atlantic. *Geobiology* 14, 54-67.

Planavsky, N.J., Reinhard, C.T., Wang, X., Thomson, D., McGoldrick, P., Rainbird, R.H., Johnson, T., Fischer, W.W., Lyons, T.W. (2014) Low mid-Proterozoic atmospheric oxygen levels and the delayed rise of animals. *Science* 346, 635-638.

Rodler, A., Sanchez-Pastor, N., Fernandez-Diaz, L., Frei, R. (2015) Fractionation behavior of chromium isotopes during coprecipitation with calcium carbonate: implications for their use as paleoclimatic proxy. *Geochimica et Cosmochimica Acta* 164, 221-235.

Scheiderich, K., Amini, M., Holmden, C., Francois, R. (2015) Global variability of chromium isotopes in seawater demonstrated by Pacific, Atlantic, and Arctic Ocean samples. *Earth and Planetary Science Letters* 423, 87-97.

Schoenberg, S., Zink, M., Staubwasser, M., von Blanckenburg, F. (2008) The stable Cr isotope inventory of solid Earth reservoirs determine by double spike MC-ICP-MS. *Chemical Geology* 249, 294-306.

Sperling, E.A., Halverson, G.P., Knoll, A.H., Macdonald, F.A., Johnston, D.T. (2013a) A basin redox transect at the dawn of animal life. *Earth and Planetary Science Letters* 371-372, 143-155.

Sperling, E.A., Frieder, C.A., Raman, A.V., Girguis, P.R., Levin, L.A., Knoll, A.H. (2013b) Oxygen, ecology, and the Cambrian radiation of animals. *Proceedings of the National Academy of Sciences USA* 110, 13446-13451.

Wedepohl, K.H. (1991) The composition of the upper Earth's crust and the natural cycles of selected metals. In: Merian, E. (Ed.) *Metals and their compounds in the environment: occurrence, analysis, and biological relevance*. VCH, Weinheim, New York, Basel, Cambridge, 3-17.

Zhang, S., Wang, X., Wang, H., Bjerrum, C.J., Hammarlund, E.U., Mafalda Costa, M., Connelly, J.N., Zhang, B., Su, J., Canfield, D.E. (2016) Sufficient oxygen for animal respiration 1,400 million years ago. *Proceedings of the National Academy of Sciences USA* 113, 1731-1736.

Oxygenation of the mid-Proterozoic atmosphere: clues from chromium isotopes in carbonates

G.J. Gilleaudeau[1,2*], R. Frei[1], A.J. Kaufman[3], L.C. Kah[4], K. Azmy[5], J.K. Bartley[6], P. Chernyavskiy[7], A.H. Knoll[8]

Supplementary Information

The Supplementary Information includes:

- Geologic Background
- Analytical Methods
- Assessment of Diagenesis
- δ^{53}Cr Correction for Detrital Influence
- Depth Relationships and δ^{53}Cr
- Figures S-1 to S-5
- Tables S-1 and S-2
- Supplementary Information References

1. Department of Geosciences and Natural Resource Management, University of Copenhagen, Øster Voldgade 10, 1350 Copenhagen, Denmark
2. Current address: School of Earth and Space Exploration, Arizona State University, Tempe, AZ 85281, USA
* Corresponding author: (email: ggillea1@gmail.com)
3. Department of Geology, University of Maryland, College Park, MD 20742, USA
4. Department of Earth and Planetary Sciences, University of Tennessee, Knoxville, TN 37996, USA
5. Department of Earth Sciences, Memorial University of Newfoundland, St. John's, Newfoundland A1B 3X5, Canada
6. Department of Geology, Gustavus Adolphus College, St. Peter, MN 56082, USA
7. Biostatistics/Radiation Epidemiology Branch, National Cancer Institute, National Institutes of Health, Rockville, MD 20850, USA
8. Department of Organismic and Evolutionary Biology, Harvard University, Cambridge, MA 02138, USA

Geologic Background

Turukhansk Uplift, Siberia

The Turukhansk Uplift succession – deposited along the northwestern edge of the Siberian craton – is comprised of thick (>4 km) unmetamorphosed carbonate and siliciclastic strata that are exposed in three thrust-bounded blocks (Petrov and Semikhatov, 1997, 1998; Sergeev, 2001). Late Mesoproterozoic rocks are separated into two distinct intervals by a regional erosional surface. Deposition in the lower interval began with the Bezymyannyi Formation, which is an open marine siliciclastic-dominated unit that accumulated near storm wave base (Petrov, 1993a; Veis and Petrov, 1994). The conformably overlying carbonate-dominated Linok Formation also accumulated near storm wave base, but palaeoenvironments shoal near the top of the unit (Petrov, 1993a,b) leading into intertidal to subtidal limestone and dolostone of the Sukhaya Tunguska Formation (Petrov *et al.*, 1995; Sergeev *et al.*, 1997). Pb-Pb geochronology on the Sukhaya Tunguska Formation yields an age of 1035 ± 60 Ma (Ovchinnikova *et al.*, 1995), which is consistent with correlations to better-dated successions elsewhere in Siberia and muted carbon isotope variability (Bartley *et al.*, 2001) that is characteristic of global carbon isotope trends in the late Mesoproterozoic Era (Kah *et al.*, 1999, 2012; Gilleaudeau and Kah, 2013a). An erosional disconformity of unknown duration sits atop the Sukhaya Tunguska Formation, above which the Derevnya Formation consists of stromatolitic (*Jacutophyton*) dolostone and shale that accumulated in an open shelf setting. Conformably overlying the Derevnya Formation is the Burovaya Formation, which accumulated along a carbonate ramp associated with stromatolitic bioherms (Petrov and Semikhatov, 1998). Carbonate of the Burovaya Formation is disconformably overlain by peritidal to shallow marine dolostone of the Shorikha Formation (Sergeev *et al.*, 1997) followed by mixed siliciclastic-carbonate deeper shelf strata of the Miroyedikha Formation (Petrov and Semikhatov, 1997). Lastly, the entire succession is overlain by the dolomitic Turukhansk Formation that accumulated in shelf settings primarily between fair weather and storm wave base (Petrov and Semikhatov, 1997). Age constraints are lacking on the units above the disconformity, although they are generally assigned to the early Neoproterozoic (~900 Ma) (Sergeev *et al.*, 1997; Sergeev, 2001). Turukhansk Uplift strata have been gently tilted (15-30°) by regional structural deformation (Bartley *et al.*, 2001), but have not been subjected to regional or contact metamorphism. Outcrop samples were collected during a joint US-Russian field expedition in 1995 (near the confluence of the Yenisei and Nizhnyaya Tunguska Rivers; ~65.8° N, 87.9° E) and samples were accessed from the archives of the Botanical Museum at Harvard University.

Angmaat Formation, Canada

The Bylot Supergroup is a thick (~6 km) succession of late Mesoproterozoic to early Neoproterozoic strata exposed within the fault-bounded Borden Basin on northern Baffin and Bylot islands, Nunavut, arctic Canada (Kah *et al.*, 1999).

Strata are divided into three unconformity-bounded sequences, and samples from this study are exclusively from the Angmaat Formation (formerly the Society Cliffs Formation), which lies at the top of the lowermost of these sequences. The dominantly dolomitic Angmaat Formation lies conformably above mixed carbonate-siliciclastic strata of the Arctic Bay and Nanisivik formations (among others; Turner and Kamber, 2012) and is, in turn, unconformably overlain by the carbonate-dominated Victor Bay Formation. Differential subsidence and graben development controlled lateral facies distribution during deposition of the Angmaat Formation (Turner and Kamber, 2012). Palaeoenvironments range from strongly evaporative, supratidal settings (recorded by direct carbonate precipitates, gypsum, and red beds in the Tay Sound outcrop section; Kah *et al.*, 1999) to subtidal settings dominated by microbial mats and ooid shoals (Milne Inlet section). The age of the Angmaat Formation is constrained by a 1199 ± 24 Ma Pb-Pb age on carbonate in the formation (Kah *et al.*, 2001), as well as a 1270 ± 4 Ma U-Pb age on subjacent volcanic rocks (Heaman *et al.*, 1992) and a U-Th-Pb whole rock age of 1092 ± 59 Ma on shale of the Arctic Bay Formation (Turner and Kamber, 2012). A late Mesoproterozoic age for the Angmaat Formation is also verified by chemostratigraphic correlation with late Mesoproterozoic strata from the Taoudeni Basin, Mauritania (Kah *et al.*, 2012). Strata have not experienced regional metamorphism, and contact metamorphism occurred only in close proximity to the Neoproterozoic Franklin swarm of mafic dykes (Turner and Kamber, 2012), which have not influenced the sections examined in this study. Outcrop samples were collected during a series of field expeditions in the mid-1990's in northernmost Baffin Island, Canada (~72.2° N, 79.5° E for the White Bay outcrop section) and samples were accessed from the archives of the Botanical Museum at Harvard University.

El Mreiti Group, Mauritania

The El Mreiti Group – deposited in the north-central Taoudeni Basin (West African craton) – is comprised of >350 metres of carbonate and siliciclastic strata that were deposited in the interior of a broad epeiric sea (Kah *et al.*, 2012; Gilleaudeau and Kah, 2013a,b, 2015). Strata are exposed in the El Mreiti region of Mauritania and are stratigraphically equivalent to pericratonic deposits of the Atar Group, which are exposed near the craton edges in the Adrar Uplift of Mauritania and to the east in Mali and Algeria. The El Mreiti Group is disconformably bounded by dominantly siliciclastic strata of the underlying Char Group and the overlying Assabet el Hassiane Group. Deposition in the El Mreiti Group began after formation of a regional peneplain and progressive marine transgression across the craton (Bertrand-Sarfati and Moussine-Pouchkine, 1988; Benan and Deynoux, 1998) – beginning with sandstone, siltstone, and shale of the Khatt Formation. Carbonate deposition began in the overlying En Nesoar Formation, which consists of intertidal to subtidal dolostone and shale. A major flooding surface is recognised at the base of the overlying Touirist Formation, above which strata are comprised of alternating clayey, stromatolitic limestone

and organic-rich shale deposited near fair weather wave base. Re-Os geochronology on organic-rich shale of the En Nesoar and Touirist formations yields ages of 1109 ± 22 Ma, 1107 ± 12 Ma, and 1105 ± 37 Ma (Rooney *et al.*, 2010), which are consistent with muted carbon isotope variability that is characteristic of global carbon isotope trends in the late Mesoproterozoic Era (Kah *et al.*, 1999, 2012; Gilleaudeau and Kah, 2013a). Palaeoenvironments shoal at the base of the overlying Aguelt el Mabha Formation, which is characterised by silty and clayey limestone deposited above fair weather wave base. Palaeoenvironments deepen again through the overlying Gouamir and Tenoumer formations, which are comprised of increasingly pure limestone deposited at or below fair weather wave base. Overlying units of the El Mreiti Group have been erosionally removed in the north-central Taoudeni Basin so that the Assabet el Hassiane Group lies disconformably above the Tenoumer Formation in the study area (Kah *et al.*, 2012; Gilleaudeau and Kah, 2013a). El Mreiti Group strata have not been subjected to regional metamorphism, and contact metamorphism is spatially confined to areas immediately adjacent to Mesozoic diabase intrusions, which do not intersect the drill core sampled in this study (Gilleaudeau and Kah, 2013a,b, 2015). Fresh core samples were collected from drill core F4 that intersected the Khatt, En Nesoar, Touirist, Aguelt el Mabha, and Gouamir formations just west of El Mreiti, Mauritania (~23.5° N, 7.85° W).

Vazante Group, Brazil

The Vazante Group – deposited along the western margin of the São Francisco craton (Minas Gerais, Brazil) – is comprised of dominantly dolomitic strata that reach up to 2 km in thickness in the eastern part of the Brasília Fold Belt (Azmy *et al.*, 2001). Vazante Group stratigraphy has recently been revised based on field observation of a thrust fault that juxtaposes late Mesoproterozoic strata above Neoproterozoic strata of the St. Antônio do Bonito and Rocinha formations (Geboy *et al.*, 2013). This observation reconciles previously documented stratigraphic inversion of U-Pb detrital zircon ages, and in this study, we focus only on Mesoproterozoic strata that lie above the fault horizon. This interval begins with the Lagamar Formation, which consists of subtidal silty dolostone with stromatolitic (*Conophyton*) horizons. This unit is overlain by organic-rich shale of the Serra do Garrote Formation, which has been dated using Re-Os geochronology at 1354 ± 88 Ma (Geboy *et al.*, 2013). Above this lies the Serra do Poco Verde and Morro do Calcario formations, which consist of relatively pure dolostone with discrete silty intervals and microbial lamination deposited in supratidal to intertidal environments (Azmy *et al.*, 2008). At the top of the Morro do Calcario Formation, a discrete diamictite interval is observed that consists of both rounded and angular cobbles and boulders that are often faceted, as well as dropstone-laden mudstone containing pseudomorphs of glendonite – a cold water carbonate mineral taken as one line of evidence for a glacial origin of Vazante Group diamictites (Olcott *et al.*, 2005; Geboy *et al.*, 2013). The base of the diamictite interval erosionally incises underlying strata, and in some cases, two

separate diamictite intervals are observed (one at the top of the Serra do Poco Verde Formation), although these relationships seem to be regionally variable (Olcott *et al.*, 2005; Azmy *et al.*, 2009; Geboy *et al.*, 2013). Re-Os geochronology on organic-rich diamictite horizons yields ages of 1100 ± 77 Ma (Azmy *et al.*, 2008) and 1112 ± 50 Ma (Geboy *et al.*, 2013), supporting a late Mesoproterozoic age for the Vazante Group. Disconformably overlying the Morro do Calcario Formation is post-glacial subtidal argillaceous dolostone of the Lapa Formation, which represents the top of the Vazante Group succession. During the Brasiliano-Pan African orogeny, regional metamorphism did not exceed lowermost greenschist facies (Azmy *et al.*, 2008) and evidence for contact metamorphism is absent in the study area. Fresh core samples were collected from drill cores CMM-500, CMM-279, and MASW-01 that intersected the Serra do Poco Verde, Morro do Calcario, and Lapa formations northwest of Unaí, Brazil (~16.3° S, 47.1° W).

Analytical Methods

Sample preparation

Outcrop and drill core samples were first slabbed using a diamond saw in order to remove weathered surfaces. Slabs were then washed in 2 M HCl to etch the surfaces that had been in contact with the saw blade. Next, slabs were wrapped in plastic and crushed to chips manually with a hammer, with the plastic wrapping designed to avoid contact of samples with the hammer. Lastly, rock chips were crushed to a fine powder using an agate mixer mill.

Chromium separation

Using modifications on a previously described procedure (Frei *et al.*, 2011), ~1 gram of powdered sample was spiked with ^{50}Cr-^{54}Cr double spike (Schoenberg *et al.*, 2008) to a 4:1 sample to spike Cr ratio. Spiked samples were then dissolved for ~30 minutes in either 0.5 M or 2 M HCl with the sample mixed through the acid using a shaker table. After dissolution, samples were centrifuged to remove insoluble residue and the supernatant was pipetted into a Teflon beaker that was pre-cleaned with aqua regia. Teflon beakers were placed uncovered on a hot plate and the supernatant was dried down overnight at 120 °C. Next, the sample was re-dissolved in aqua regia (made from double-distilled HCl and HNO_3) and, again, dried down overnight at 120 °C to ensure sample/spike homogenisation. Samples were then re-dissolved in 0.1 M HCl, and ~1 mL of $(NH_4)S_2O_8$ was added to each beaker as an oxidising agent. Beakers were capped and heated in a microwave for ~30 minutes (or until boiling was observed) to oxidise Cr(III) to Cr(VI). Oxidised samples were then passed over an anion exchange column charged with 2 mL of Dowex AG 1 × 8 anion resin (100-200 mesh, pre-conditioned with 6 M HCl), during which Cr(VI)-oxyanions are adsorbed to the resin surface by exchange with chloride ions. Cr was then released from the anion resin by reduction to Cr(III) using 2 M double-distilled HNO_3 and H_2O_2. The resulting liquid

was dried down overnight at 120 °C and the sample was re-dissolved in 1 mL of 6 M double-distilled HCl before being passed over a second anion exchange column – also charged with 2 mL of Dowex AG 1 × 8 anion resin (100-200 mesh, pre-conditioned with 6 M HCl) – designed specifically for removal of iron (Fe). Fe removal is critical because of isobaric interference between ^{54}Fe and ^{54}Cr during isotopic analysis. Again, the resulting liquid was dried down overnight at 120 °C and samples were re-dissolved in 200 µL of 6 M double-distilled HCl. After dilution with 2.2 mL of ultrapure MQ water, samples were passed over a cation exchange column charged with 2 mL of Dowex AG50W-X8 cation resin (200-400 mesh, pre-conditioned with 0.5 M HCl). Cation exchange is used to separate Cr from major matrix elements such as Ca, Mg, Mn, Al, and residual Fe. The resulting liquid was dried down overnight at 120 °C and the precipitate was then ready for loading onto a Re filament for Cr-isotopic analysis.

Thermal ionisation mass spectrometry (TIMS)

All Cr-isotope measurements were performed at the University of Copenhagen on an IsotopX Ltd. IsoProbe T or Phoenix thermal ionisation mass spectrometer (TIMS) equipped with eight Faraday collectors that allow simultaneous collection of all four chromium beams ($^{50}Cr^+$, $^{52}Cr^+$, $^{53}Cr^+$, $^{54}Cr^+$) together with $^{49}Ti^+$, $^{51}V^+$, and $^{56}Fe^+$ as monitors for small interferences from other isotopes of these same elements. Final precipitates after Cr separation were loaded onto outgassed Re filaments along with a mixture of 3 µL of silicic acid, 1 µL of 0.5 M H_3BO_3, and 1 µL of 0.5 M H_3PO_4. Samples were analysed at temperatures ranging from 1000-1250 °C with ^{52}Cr beam intensities between 200 and 1000 mV. One run consisted of 120 cycles (grouped into 24 blocks of 5 cycles each with 10 second signal integration periods) and at least two (but as many eight) runs were performed for each sample. The final isotopic composition of a sample is reported as the average of these repeated analyses with standard errors reported as the standard deviation (s.d.) of isotopic values divided by the square root of n (the number of runs). Isotopic compositions are reported in per mil (‰) notation relative to the certified Cr-isotope standard NIST SRM 979:

$$\delta^{53}Cr\ (‰) = ((^{53}Cr/^{52}Cr_{sample})/(^{53}Cr/^{52}Cr_{\ NIST\ SRM\ 979}) - 1) \bullet 1000 \quad \text{Eq. S-1}$$

Standard errors for our samples were consistently <0.05 ‰. Initial sample and spike weights were also used to determine the Cr concentration of each sample (in ppm) from TIMS data. Blanks produced consistently <15 ng of Cr, which is negligible compared to our samples that contained between ~500 ng and 6 µg of Cr.

The external reproducibility of our measurements was assessed by comparing long-term average $\delta^{53}Cr$ values for NIST SRM 979 and NIST 3112a measured on the IsoProbe T and the Phoenix to accepted values from other laboratories (Schoenberg *et al.*, 2008). Our results over >5 years of analysis indicate that standard values are measured 0.09 ‰ lower on the IsoProbe T and 0.08 ‰ higher on the Phoenix compared to accepted values. As a result, 0.09 ‰ was added to raw $\delta^{53}Cr$ values produced on the IsoProbe T and 0.08 ‰ was subtracted

from raw δ^{53}Cr values produced on the Phoenix. During the course of the runs presented in this study, NIST SRM 979 and NIST 3112a values were reproduced with analytical uncertainties <0.05 ‰. Internal reproducibility was assessed by dissolving certified carbonate standards JLs-1 (Triassic limestone) and JDo-1 (Permian dolostone) and measuring their Cr-isotopic composition along with samples from each run. Measured δ^{53}Cr values were +1.80 ± 0.06 ‰ for JLs-1 and +1.64 ± 0.03 ‰ for JDo-1, both of which are in good agreement with published values (Schoenberg *et al.*, 2008).

Major and trace element abundances

Ca, Mg, Fe, Sr, Mn, and Al concentrations were measured by ICP-OES at the University of Copenhagen on splits of the same sample solutions used for Cr-isotopic analysis. Solutions were diluted with 2 % HNO_3 to a Ca concentration of ~50 ppm, and limestone and dolostone samples were analysed separately along with three separate calibration solutions designed to mimic the range of element concentrations expected in limestone and dolostone samples. Duplicates of certified carbonate standards (JLs-1 and JDo-1) were measured every nine samples and analytical precision was determined using the reproducibility of molar element to Ca ratios in the standards. Measured values are in good agreement with published values for both JLs-1 and JDo-1. The sum of cation concentrations relative to initial sample weight was used to determine the carbonate content of each sample. Carbonate content was then used to correct measured concentrations of Ca, Mg, Fe, Sr, and Mn to reflect concentrations specifically in carbonate. Ti and Zr abundances were measured by ICP-MS at the Geological Survey of Denmark and Greenland (GEUS). 25-35 mg of sample powder was dissolved in 2 mL of either 0.5 M or 2 M HCl and final solutions were diluted up to 10 mL with ultrapure MQ water. Samples were analysed using the USGS BHVO-1 (basalt, Hawaiian Volcanic Observatory) standard as a reference material along with dissolved carbonate standards (JLs-1 and JDo-1). Measured Ti and Zr concentrations for the BHVO-1 standard are in good agreement with published values.

Assessment of Diagenesis

Petrography

Conventional petrography in plane- and cross-polarised light was used as a first measure of diagenesis in the carbonate successions investigated in this study. Primary and early diagenetic carbonate matrix phases are fine-grained (micritic to microsparitic) and lack planar, interlocking grain boundaries (Longman, 1980). By contrast, meteoric or deep burial diagenesis – in the presence of fluids different in composition than primary marine fluids – produces coarse-grained spar that often exhibits planar, interlocking grain boundaries, with the exception of grain micritisation processes that can produce fine-grained carbonate

phases through recrystallisation and infilling of endolithic microborings (Reid and Macintyre, 1998). Additionally, dolomitisation can occur during a variety of diagenetic stages that can also be identified petrographically (Tucker, 1983). If dolomite forms during early diagenesis in the presence of marine fluids, primary textural characteristics are commonly retained (*i.e.* fabric-retentive dolomitisation). Early replacement by thermodynamically stable dolomite can act to buffer carbonate systems against subsequent diagenesis and overprinting of geochemical signatures (Nicholas, 1996). By contrast, dolomite formed during deep burial diagenesis (or in contact with hydrothermal fluids) commonly obliterates primary textural characteristics, replacing them with coarse, euhedral or saddle dolomite (*i.e.* fabric-destructive dolomitisation).

In the El Mreiti Group, micritic to microsparitic fabrics dominate limestone of the Touirist, Aguelt el Mabha, and Gouamir formations (Fig. S-1a), with Gouamir samples occasionally exhibiting neomorphic crystal fans formed during early diagenesis (Gilleaudeau and Kah, 2013a). By contrast, original carbonate fabrics in the En Nesoar Formation have been partially replaced by fabric-destructive, zoned, euhedral dolomite (Fig. S-1b) indicating a later stage of diagenesis during burial. It is hypothesised (Gilleaudeau and Kah, 2013a) that the flooding surface marking the base of the Touirist Formation served as a conduit for later fluid flow that affected carbonate preservation in the En Nesoar and basal Touirist formations. Samples from this stratigraphic interval are excluded from further consideration.

In the Turukhansk Uplift succession, limestone of the Linok, Sukhaya Tunguska, and Burovaya formations is uniformly micritic with no evidence for recrystallisation in the presence of non-marine fluids (Bartley *et al.*, 2001). Limestone of the Miroyedikha Formation exhibits a range of petrographic fabrics that indicate varying degrees of recrystallisation (Bartley *et al.*, 2001). The majority of samples are characterised by fine-grained, clotted, micritic fabrics (Fig. S-1c) with a few notable exceptions – an interval with partially recrystallised and heavily stylolitised intraclasts (Fig. S-1d) and an interval with coarse, fabric-destructive, euhedral dolomite (Fig. S-1e). Samples from these two discrete intervals are excluded from further consideration. The Turukhansk Formation is characterised by fine-grained fabric-retentive dolomite that precipitated during very early diagenesis (Knoll *et al.*, 1995), resulting in pervasive clotted micritic fabrics similar to well-preserved intervals of the Miroyedikha Formation (Fig. S-1c). Coarse competitive-growth dolomite cements are observed in some samples, but overall they comprise <10 % of the rock by volume.

The Vazante Group, the Serra do Poco Verde, Morro do Calcario, and Lapa formations are all characterised by uniformly micritic to microsparitic, fabric-retentive dolomite (Azmy *et al.*, 2001) that precipitated during very early diagenesis (Fig. S-1f). Some samples are characterised by a complex set of dolomite cements that span from early diagenetic, bladed crystals to late diagenetic, interlocking, void-filling cements (Fig. S-1f). Cement phases comprise <20 % of the rock by volume (Azmy *et al.*, 2001), however, and have been visually avoided for sampling in this study.

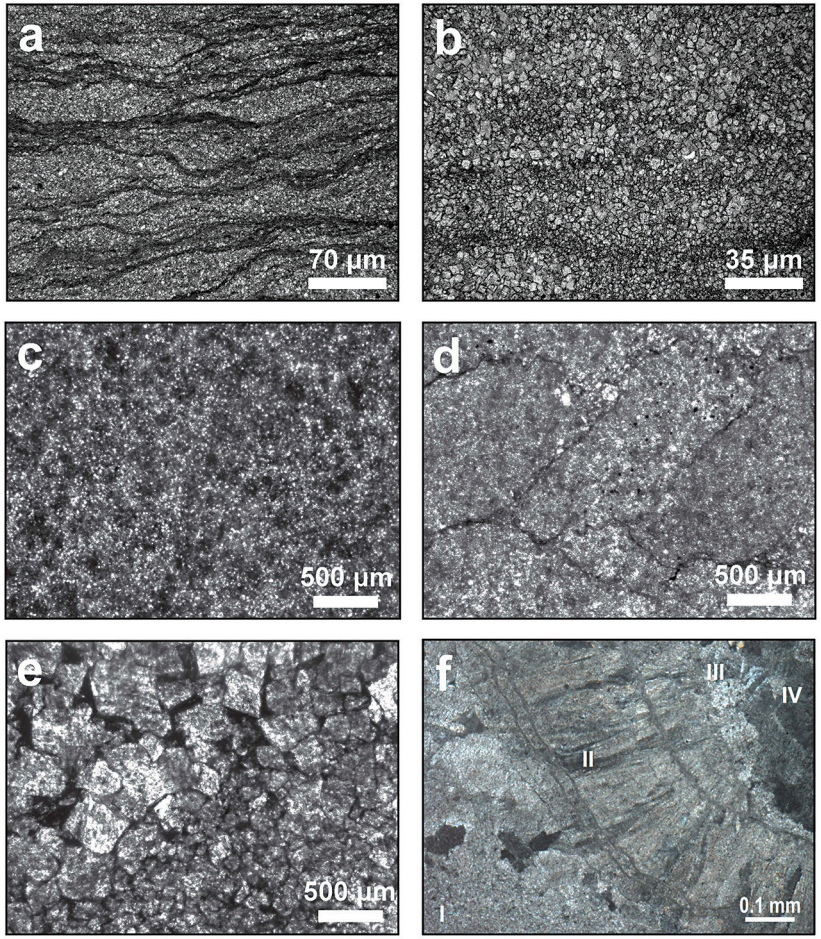

Figure S-1 Photomicrographs highlighting specific textural features in the **(a,b)** El Mreiti Group, **(c,d,e)** Turukhansk Uplift, and **(f)** Vazante Group. **(a)** Typical micritic limestone of the Touirist Formation. **(b)** Interval of fabric-destructive dolomitisation in the En Nesoar Formation. **(c)** Typical clotted micritic limestone of the Miroyedikha Formation. **(d)** Stylolitised and partially recrystallised intraclasts from the Miroyedikha Formation. **(e)** Coarse dolomitic spar filling inter-stromatolitic voids in the Miroyedikha Formation. **(f)** Fine-grained fabric-retentive dolomite (I) of the Lapa Formation (Vazante Group) surrounded by multiple stages (II, III, IV) of later dolomitic cements (>80 % by volume of the Lapa Formation consists of phase I dolomite).

In the Angmaat Formation, fabric retentive dolomitisation during early diagenesis has preserved a range of primary textures (Fig. S-2). These include storm microbreccias and evaporative structures (tepee structures and gypsum

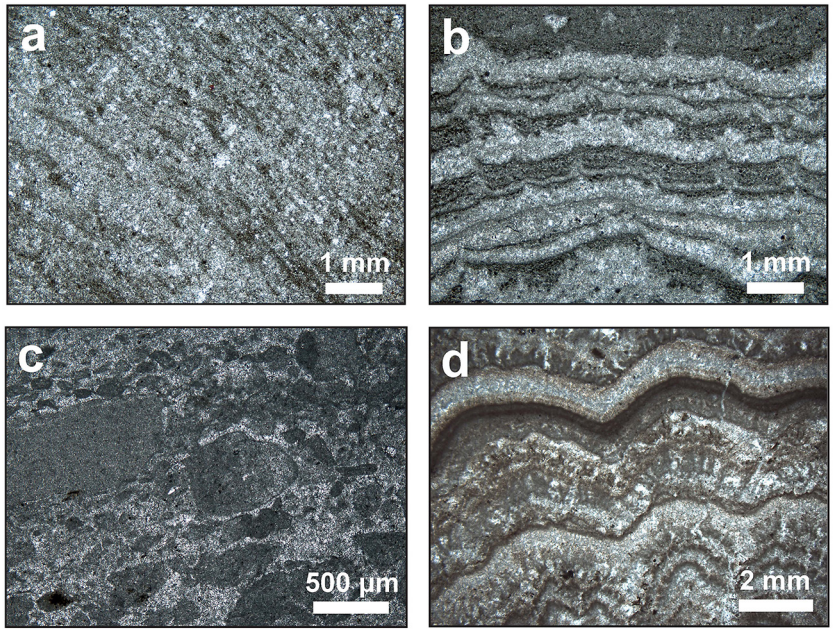

Figure S-2 Photomicrographs highlighting textural characteristics of the Angmaat Formation. A variety of primary depositional fabrics have been preserved through early dolomitisation, including evaporative features and tepee structures, a storm microbreccia, and microbial mats.

pseudomorphs), as well as a range of microbial fabrics, including finely laminated and tufted mats, along with clotted microbialites. Dolomite crystal sizes range from micrite to microspar with no evidence for coarse recrystallisation during later diagenesis, aside from occasional void-filling cements that were avoided for sampling in this study.

Carbon/oxygen isotopes and trace element signatures

The carbon/oxygen isotope and trace element composition of each sample was also used as a monitor of diagenetic alteration. Both $\delta^{13}C$ and $\delta^{18}O$ can be altered by meteoric and/or burial diagenesis, with $\delta^{18}O$ being more susceptible to alteration because the $\delta^{13}C$ value of diagenetic fluids often becomes buffered to rock values (Banner and Hanson, 1990). $\delta^{13}C$ and $\delta^{18}O$ are both commonly lowered through diagenesis, although higher $\delta^{18}O$ values can be imparted through interaction with saline burial fluids (Dorobek, 1987). Well-preserved Proterozoic limestones and dolostones typically have $\delta^{18}O$ values between –6 and –10 ‰ (Bartley *et al.*, 2007; Kah *et al.*, 2012; Gilleaudeau and Kah, 2013a), providing a benchmark by which to assess the preservation of our samples.

The concentration of Sr, Fe, and Mn in the carbonate lattice can also be a sensitive monitor for diagenetic processes (Banner and Hanson, 1990; Ullmann and Korte, 2015). Primary marine limestone readily incorporates Sr, which is then easily expelled from the crystal lattice during recrystallisation. By contrast, limestone deposited under normal marine conditions is normally depleted in Fe and Mn because of the insolubility of these elements in oxic seawater. Limestone can then become enriched in Fe and Mn if recrystallisation occurs in the presence of reducing burial fluids. In light of these observations, Mn/Sr ratios have become a standard measure of diagenesis in carbonate strata, with higher Mn/Sr ratios indicating Mn-enrichment and Sr-depletion through diagenetic alteration. Mn/Sr >10 is considered altered (Kaufman and Knoll, 1995), although potentially higher Fe and Mn concentrations in low-oxygen Proterozoic oceans suggest that the use of absolute numerical cutoff values is not appropriate in many cases (Gilleaudeau and Kah, 2013a). The same principles of Sr, Fe, and Mn incorporation apply to dolostones, with the caveat that the dolomite crystal lattice has a lower preference for Sr (Vahrenkamp and Swart, 1990) and a higher preference for Fe and Mn (Mazzullo, 1992) than calcite. As a result, we emphasise the recognition of diagenetic trends within carbonate trace element data instead of the use of absolute cutoffs for sample inclusion.

In the El Mreiti Group, Touirist, Aguelt el Mabha, and Gouamir formations, samples have geochemical signatures typical of well-preserved Proterozoic limestone (Mn/Sr <10; $\delta^{18}O$ from –6 to –10 ‰; Fig. S-3), consistent with petrographic evidence for fine-grained micritic to microsparitic calcite phases. In the En Nesoar Formation, however, elevated Mn/Sr ratios (>15) and ^{18}O enrichment (Gilleaudeau and Kah, 2013a; Fig. S-3) are also consistent with petrographic evidence for late, fabric-destructive dolomitisation, supporting our exclusion of these samples from further consideration.

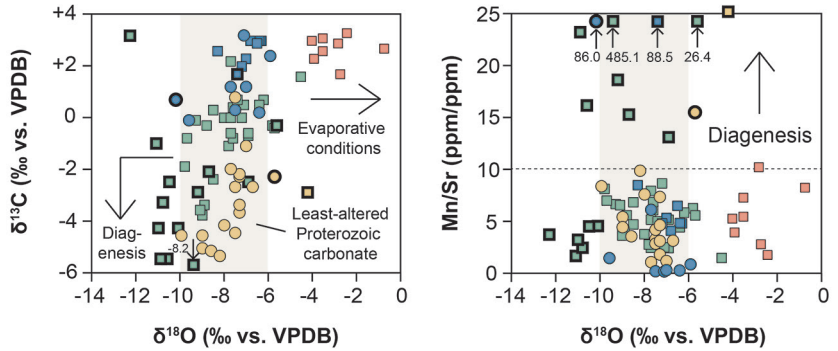

Figure S-3 Geochemical indicators of diagenesis in all four sections. Circles are limestone and squares are dolostone. Bold points represent samples that were excluded from further discussion based on diagenetic criteria. Blue = Turukhansk, red = Angmaat, tan = El Mreiti, and green = Vazante.

In the Turukhansk Uplift succession, limestone of the Linok, Sukhaya Tunguska, and Burovaya formations has Mn/Sr ratios <1.5 and $\delta^{18}O$ values typical of well-preserved Proterozoic limestone (generally –6 to –10 ‰; Fig. S-3) – consistent with petrographic observations of primarily micritic phases. Limestone of the Miroyedikha Formation has undergone varying degrees of recrystallisation and those samples with obvious petrographic evidence for recrystallisation (Fig. S-1) also have anomalously high Mn/Sr ratios (>85), supporting our exclusion of these samples. In the Turukhansk Formation, there is a tight range of Mn/Sr ratios <8.5 and $\delta^{18}O$ values between –6 and –8.5 ‰ (Fig. S-3), which is consistent with early fabric-retentive dolomitisation.

In the Vazante Group, isotopic and elemental trends suggest the potential for some later diagenetic alteration despite the dominance of micritic fabrics throughout the succession. A cross-plot of $\delta^{13}C$ *vs.* $\delta^{18}O$ values (Fig. S-3) reveals some samples that are depleted in both ^{13}C and ^{18}O relative to the rest of the succession. These samples also sometimes exhibit elevated Mn/Sr ratios (>10), prompting us to exclude these samples from further consideration based on two independent lines of geochemical evidence.

In the Angmaat Formation, petrographic evidence for early dolomitisation that preserved original fabrics (Fig. S-2) is in good agreement with isotopic and elemental data. Despite the lower preference of dolomite for Sr in the crystal lattice (Vahrenkamp and Swart, 1990), Mn/Sr ratios are uniformly <10 (commonly <5), excluding one sample (Mn/Sr = 10.33). Carbon isotopic values are stratigraphically coherent (Kah *et al.*, 1999) and in good agreement with globally recognised late Mesoproterozoic carbon isotope signals (Kah *et al.*, 2012). Oxygen isotope compositions in the Angmaat Formation are ^{18}O-enriched compared to most well-preserved Proterozoic carbonates, however (Fig. S-3). This is due to the evaporative nature of depositional fluids in the Borden Basin, which is supported by the presence of bedded gypsum and sedimentological features such as tepee structures (Kah *et al.*, 2001). Thus, the oxygen isotope signature of Angmaat Formation dolostones is not taken as evidence for late diagenetic alteration.

In total, 17 samples were excluded based on petrographic and geochemical signs of diagenetic alteration. The remaining samples fit all standard criteria for well-preserved carbonate and we emphasise that isotopic and trace element signatures mimic petrographic observations, thus providing multiple independent lines of evidence that support our criteria for sample inclusion.

The only previously published study on Cr-isotopes in carbonate rocks (Frei *et al.*, 2011) demonstrated stratigraphic $\delta^{53}Cr$ trends that mirror primary $\delta^{13}C$ trends across a mixed limestone-dolostone interval. Because the C-isotope signal is thought to reflect seawater, co-variation with $\delta^{53}Cr$ speaks to the potential fidelity of Cr-isotopes in both limestone and dolostone and suggests that, in the absence of further study on Cr-isotope behaviour during diagenesis, standard petrographic and geochemical criteria can be used as a starting point for Cr-isotope diagenetic screening.

δ^{53}Cr Correction for Detrital Influence

In addition to reporting raw δ^{53}Cr values determined by TIMS, we also used sample Cr/Al ratios compared to average detrital sediment – using average shale composition as a proxy (Cr = 90 ppm; Al = 88,900 ppm) (Wedepohl, 1991) – to determine the fraction of Cr sourced from detrital material for each sample. The calculated fraction of detrital Cr was then used to separate the isotopic composition of authigenic Cr in carbonate from the isotopic composition of detrital Cr, which is derived from average crustal values (–0.123 ± 0.102 ‰) (Schoenberg *et al.*, 2008). First, the concentration (in ppm) of detrital Cr leached during sample dissolution ($[Cr]_{det}$) was determined using:

$$[Cr]_{det} = [Cr]_{avgsh} \bullet ([Al]_{sample}/[Al]_{avgsh}) \quad \text{Eq. S-2}$$

In this equation, we set $[Cr]_{avgsh}$ = 90 ppm and $[Al]_{avgsh}$ = 88,900 ppm based on average shale values (Wedepohl, 1991). Next, the concentration (in ppm) of authigenic Cr ($[Cr]_{auth}$) was determined using:

$$[Cr]_{auth} = [Cr]_{sample} - [Cr]_{det} \quad \text{Eq. S-3}$$

Next, we determined the percentage of detrital Cr measured with each isotopic analysis using:

$$\%_{det\ Cr} = [Cr]_{det}/([Cr]_{sample}/100) \quad \text{Eq. S-4}$$

Lastly, we determined the isotopic composition of the authigenic Cr component ($\delta^{53}Cr_{auth}$) using:

$$\delta^{53}Cr_{auth} = \delta^{53}Cr_{raw} \bullet (\%_{detCr}/100) \bullet [Cr]_{det} + (1 - (\%_{detCr}/100)) \bullet [Cr]_{auth}) - (\delta^{53}Cr_{det} \bullet [Cr]_{det} \bullet (\%_{detCr}/100)))/([Cr]_{auth} \bullet (1 - (\%_{detCr}/100)) \quad \text{Eq. S-5}$$

In this equation, we set $\delta^{53}Cr_{det}$ = –0.123 based on average crustal values (Schoenberg *et al.*, 2008). Our dataset reveals that when the detrital Cr component ($\%_{detCr}$) exceeds ~35 % of total measured Cr, the isotopic composition of the authigenic seawater component is unresolvable, and correction values are not reported in this study. We also performed corrections using post-Archaean Australian shale (PAAS) values (Taylor and McLennan, 1985) instead of the average shale composite of Wedepohl (1991), but found <2 % differences in estimates of detrital Cr contribution and <0.02 ‰ differences in corrected $\delta^{53}Cr_{auth}$ values.

Depth Relationships and δ^{53}Cr

In addition to fluctuations in atmospheric pO_2, $\delta^{53}Cr_{auth}$ heterogeneity in our dataset is likely to reflect internal redox cycling of Cr in marine environments. In the modern ocean, Cr-isotope heterogeneity occurs with depth controlled by biologically-mediated Cr-reduction in surface waters and the oxygen minimum zone, as well as re-oxidation of Cr(III) in deep water (Scheiderich *et al.*, 2015). To investigate potential depth relationships in our dataset, samples were binned into five categories of relative water depth based on sedimentary facies (supratidal; intertidal to shallow subtidal; above fair weather wave base (FWWB); between

FWWB and storm wave base (SWB); and below SWB). An ANOVA was used to compare their mean δ^{53}Cr values recognising that these environments were not sampled contemporaneously. Of ten possible pair-wise mean differences, only one was found to be statistically significant (between supratidal (n = 4) and environments above FWWB (n = 3)). This difference was not deemed practically significant, however, because of the small sample size for each environment. In summary, we found no appreciable differences in δ^{53}Cr associated with depositional water depth. Lack of depth dependence is likely related to a high degree of redox heterogeneity in shallow mid-Proterozoic environments (*i.e.* Gilleaudeau and Kah, 2013b, 2015), influencing the degree of *in situ* Cr-reduction.

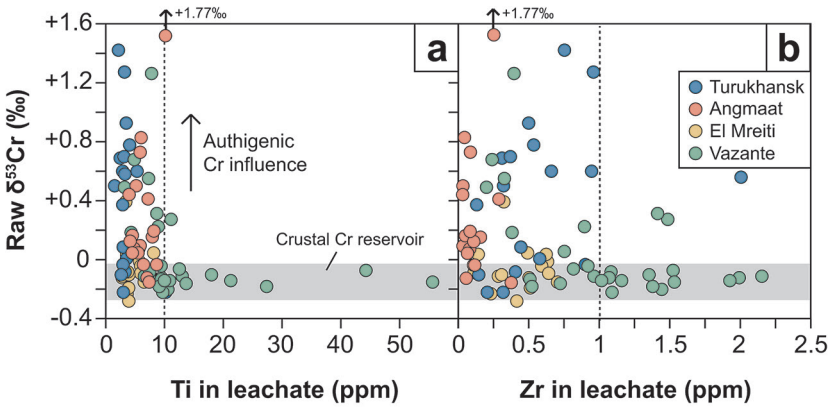

Figure S-4 Cross-plots of raw Cr-isotope values *vs.* other detrital indicators (Ti and Zr). Dashed lines represent 10 ppm Ti and 1 ppm Zr, which seem to be the cutoff values above which detrital Cr masks the authigenic Cr-isotope signal.

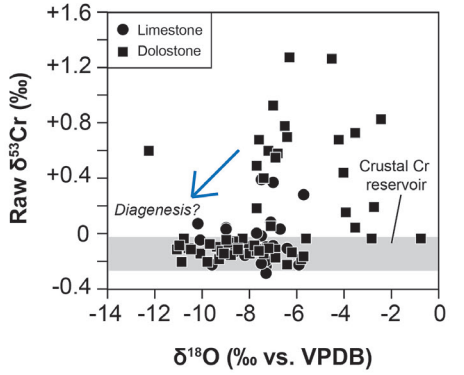

Figure S-5 Cross-plot of raw Cr-isotope values and O-isotopes indicating that lower O-isotope values (potentially indicating diagenesis) correspond to unfractionated Cr-isotope values. This could mean that diagenetic alteration (at least in the case of the Vazante Group) has the potential to reset Cr-isotopes to crustal values.

Table S-1 Sample information, mineralogy, Cr-isotope, and Al concentration data for carbonates from the Turukhansk Uplift, Vazante and El Mreiti groups, and the Angmaat Formation (~1.1 to 0.9 Ga).

Sample	Core/ Outcrop	Formation	Mineralogy	Cr (ppm)	$\delta^{53}Cr_{raw}$ (‰)	Std. error (‰)	% detrital Cr	$\delta^{53}Cr_{auth}$ (‰)	Al (ppm)	Cr/Al x 1000
TURUKHANSK										
K95-9	KAM	Linok	LS	1.64	-0.23	0.04	23.1	-0.24	343	4.77
K95-22	KAM	Sukh. Tung.	LS	0.21	-0.22	0.03	16.9	-0.23	33	6.5
K95-76	ST	Sukh. Tung.	LS	0.31	-0.11	0.03	21.5	-0.11	60	5.12
K95-86	ST	Sukh. Tung.	LS	0.21	0.08	0.06	14	0.08	27	7.87
K95-88-1	ST	Sukh. Tung.	LS	0.39	0.37	0.05	3.8	0.37	13	29.21
K95-38	KAM	Burovaya	LS	0.65	-0.23	0.05	21.7	-0.24	128	5.07
K95-129-175	MIR	Miroyedikha	LS	0.56	-0.09	0.02	22.4	-0.08	113	4.91
K95-140-34	YEN	Miroyedikha	LS	0.64	0.69	0.05	15.7	0.72	91	6.99
K95-140-38	YEN	Miroyedikha	LS	1.19	0	0.03	22.8	0.01	246	4.82
K95-140-43	YEN	Miroyedikha	LS	0.57	0.5	0.04	14.2	0.52	74	7.74
K95-140-155	YEN	Miroyedikha	DS	0.98	0.93	0.03	15.1	0.97	135	7.27
K95-140-177	YEN	Miroyedikha	DS	1.61	0.6	0.04	16.7	0.63	245	6.58
K95-142-1	YEN	Turukhansk	DS	1.28	1.28	0.02	19.5	1.36	227	5.65
K95-142-15	YEN	Turukhansk	DS	1.02	0.6	0.05	18.5	0.63	171	5.94
K95-142-20	YEN	Turukhansk	DS	1.1	0.7	0.03	14.3	0.72	143	7.7
K95-142-25	YEN	Turukhansk	DS	1.3	1.43	0.05	5.9	1.44	70	18.66
K95-142-30	YEN	Turukhansk	DS	1.24	0.58	0.03	12.1	0.59	137	9.06
K95-142-60	YEN	Turukhansk	DS	1.74	0.78	0.05	14.8	0.81	234	7.45
K95-142-65	YEN	Turukhansk	DS	1.03	-0.04	0.04	17.9	-0.04	167	6.16
K95-140-48	YEN	Miroyedikha	DS	1.46	0.4	0.02	15.9	-	210	6.94
K95-140-126	YEN	Miroyedikha	LS	1.53	0.07	0.07	25.5	-	354	4.32
VAZANTE										
KV 500 3	CMM-500	Ser. do P.Ver.	DS	1.18	0.55	0.08	31.4	0.69	337	3.5
KV 279 05	CMM-279	Mor. do Calc.	DS	4.42	1.27	0.09	3.7	1.27	148	29.88
KV 279 12	CMM-279	Mor. do Calc.	DS	0.38	0.7	0.09	33.4	0.91	115	3.3
KV 279 11	CMM-279	Mor. do Calc.	DS	0.79	0.18	0.08	47.7	-	342	2.31
KV 279 01	CMM-279	Mor. do Calc.	DS	1.34	0.49	0.07	13.7	0.51	167	8.02
MAS 1006	MASW 01	Lapa	DS	6.62	0.31	0.08	6.7	0.31	404	16.38
MAS 1002.5	MASW 01	Lapa	DS	4.56	0.27	0.08	15.4	0.28	638	7.15
MAS 94	MASW 01	Lapa	DS	4.92	0.22	0.07	8.5	0.22	380	12.96
MAS 92	MASW 01	Lapa	DS	0.54	0.68	0.05	34.2	0.9	168	3.21
MAS 86	MASW 01	Lapa	DS	1.09	-0.07	0.06	59.6	-	590	1.85
MAS 83	MASW 01	Lapa	DS	0.98	-0.05	0.06	47.4	-	422	2.32
MAS 82	MASW 01	Lapa	DS	0.54	-0.11	0.07	100	-	1012	0.53
MAS 81	MASW 01	Lapa	DS	0.66	-0.15	0.04	76.7	-	460	1.44
MAS 73	MASW 01	Lapa	DS	2.32	-0.19	0.08	16.5	-0.19	347	6.68
MAS 72	MASW 01	Lapa	DS	2.77	-0.17	0.05	19.5	-0.17	491	5.64
MAS 70	MASW 01	Lapa	DS	2.57	-0.14	0.05	12.9	-0.14	302	8.51
MAS 69	MASW 01	Lapa	DS	5.6	-0.23	0.07	15.1	-0.23	770	7.28
MAS 60	MASW 01	Lapa	DS	1.59	-0.15	0.08	67.2	-	970	1.64
MAS 57	MASW 01	Lapa	DS	0.87	-0.11	0.08	72.2	-	571	1.52
MAS 52	MASW 01	Lapa	DS	4.04	-0.16	0.06	35.6	-0.17	1306	3.09
MAS 46	MASW 01	Lapa	DS	3.15	-0.15	0.06	24.6	-0.15	704	4.47
MAS 38	MASW 01	Lapa	DS	1.08	-0.08	0.06	100	-	1599	0.68
MAS 22	MASW 01	Lapa	DS	4.34	-0.19	0.06	27.4	-0.2	1081	4.01
MAS 16	MASW 01	Lapa	DS	0.87	-0.12	0.06	100	-	1531	0.57
MAS 13	MASW 01	Lapa	DS	3.63	-0.13	0.05	15.2	-0.13	502	7.24
MAS 08	MASW 01	Lapa	DS	0.8	-0.21	0.06	50.9	-	370	2.16
MAS 07	MASW 01	Lapa	DS	1.22	-0.09	0.06	30.1	-0.08	334	3.66
MAS 06	MASW 01	Lapa	DS	1.2	0.05	0.07	28.4	0.08	310	3.87
MAS 04	MASW 01	Lapa	DS	0.98	-0.12	0.06	25.3	-0.12	226	4.34
MAS 02	MASW 01	Lapa	DS	0.89	-0.13	0.08	55.2	-	447	1.99
KV 279 13	CMM-279	Mor. do Calc.	DS	0.72	0.6	0.08	18.2	-	119	6.04
MAS 87	MASW 01	Lapa	DS	2.11	-0.1	0.07	100	-	2992	0.71
MAS 80	MASW 01	Lapa	DS	1.09	-0.11	0.07	81.6	-	808	1.35
MAS 79	MASW 01	Lapa	DS	0.48	-0.06	0.09	73.5	-	321	1.5
MAS 78	MASW 01	Lapa	DS	1.26	-0.21	0.07	76.7	-	878	1.43
MAS 77	MASW 01	Lapa	DS	0.69	-0.13	0.08	100	-	1297	0.53
MAS 76	MASW 01	Lapa	DS	1.36	-0.04	0.06	19.6	-	242	5.63
MAS 74	MASW 01	Lapa	DS	1.42	-0.18	0.05	100	-	1717	0.83
MAS 30	MASW 01	Lapa	DS	2.23	-0.12	0.08	33.4	-	677	3.29
MAS 12	MASW 01	Lapa	DS	0.98	-0.15	0.07	78.7	-	701	1.4
MAS 11	MASW 01	Lapa	DS	0.96	-0.04	0.06	74.3	-	648	1.48
MAS 10	MASW 01	Lapa	DS	1.67	-0.09	0.08	45	-	684	2.44
MAS 09	MASW 01	Lapa	DS	1.48	-0.12	0.07	30.8	-	415	3.57
EL MREITI										
F4-48	F4	Touirist	LS	1.67	0.39	0.01	16.1	0.41	245	6.81
F4-80	F4	Ag. el Mabha	LS	1.38	0.04	0.09	85	-	1063	1.29
F4-87	F4	Ag. el Mabha	LS	1.8	-0.13	0.06	35.9	-0.13	588	3.06
F4-89	F4	Ag. el Mabha	LS	1.06	-0.02	0.04	88.2	-	849	1.25
F4-90	F4	Ag. el Mabha	LS	0.8	0.03	0.06	67.1	-	490	1.64
F4-92	F4	Ag. el Mabha	LS	1.05	-0.16	0	89.6	-	855	1.23
F4-95	F4	Ag. el Mabha	LS	1.16	-0.05	0.03	77	-	809	1.43
F4-97	F4	Ag. el Mabha	LS	0.94	-0.1	0.05	73.5	-	628	1.5

Sample	Core/ Outcrop	Formation	Miner-alogy	Cr (ppm)	$\delta^{53}Cr_{raw}$ (‰)	Std. error (‰)	% detrital Cr	$\delta^{53}Cr_{auth}$ (‰)	Al (ppm)	Cr/Al x 1000
F4-99	F4	Gouamir	LS	0.75	-0.1	0.05	40.3	-	274	2.73
F4-101	F4	Gouamir	LS	0.44	-0.24	0.03	56.5	-	228	1.95
F4-105	F4	Gouamir	LS	0.68	0.03	0.02	35	0.08	216	3.14
F4-107	F4	Gouamir	LS	0.65	-0.12	0.02	57.6	-	343	1.91
F4-109	F4	Gouamir	LS	1.09	-0.29	0.04	31.8	-0.33	316	3.46
F4-111	F4	Gouamir	LS	0.67	-0.2	0.04	44.9	-	273	2.45
F4-113	F4	Gouamir	LS	0.48	-0.11	0.04	46.2	-	203	2.38
F4-115	F4	Gouamir	LS	0.6	-0.09	0.04	34.7	-0.08	191	3.17
F4-19	F4	En Nesoar	LS	2.15	0.28	0.04	9.9	-	193	11.13
F4-21	F4	En Nesoar	DS	11.05	0.68	0.03	4	-	401	27.58
ANGMAAT										
A2-37855	AR	Angmaat	DS	0.73	0.15	0.02	15	0.16	99	7.34
MI-27390	MI	Angmaat	DS	0.25	0.07	0.05	14.3	0.08	32	7.67
MI-27450	MI	Angmaat	DS	0.19	0.09	0.09	28	0.12	48	3.92
MI-3420	MI	Angmaat	DS	0.18	0.16	0.02	24.4	0.19	39	4.51
TY-13	TS	Angmaat	DS	0.13	0.07	0.03	27.6	0.1	34	3.98
TY-18025B	TS	Angmaat	DS	0.21	0.04	-	8.8	0.04	17	12.43
TP-24260	TS	Angmaat	DS	0.86	0.41	0.03	9.3	0.42	72	11.85
TY-3975	TS	Angmaat	DS	0.44	0.5	0.03	10.3	0.51	41	10.69
TY-4	TS	Angmaat	DS	0.8	1.77	0.03	6.9	1.78	50	15.89
WB-13284A	WB	Angmaat	DS	0.19	0.12	0.03	12.4	0.13	21	8.84
WB-3600	WB	Angmaat	DS	0.26	-0.13	0.03	26.8	-0.14	64	4.1
WB-815	WB	Angmaat	DS	0.86	-0.16	-	16.2	-0.16	127	6.79
WB2-7955	WB	Angmaat	DS	0.21	0.04	0.03	17.3	0.05	32	6.35
WB2-8765	WB	Angmaat	DS	0.6	0.19	0.06	22.6	0.22	124	4.88
WB94-12	WB	Angmaat	DS	0.41	0.73	0.12	23.3	0.8	87	4.72
WB94-14	WB	Angmaat	DS	0.44	-0.04	0.02	7.5	-0.03	30	14.76
WB94-3	WB	Angmaat	DS	0.97	0.83	0.01	0	0.83	0	-
WB94-6	WB	Angmaat	DS	0.24	0.44	0.02	16	0.46	34	6.89
WB94-16	WB	Angmaat	DS	0.4	-0.04	0.06	20.2	-0.03	73	5.45

Turukhansk Uplift outcrop sections: KAM = Kammennaya-Bol'shaya Shorikha River; ST = Sukhaya Tunguska River; MIR = Miroyedikha River; YEN = Yenisei River
Angmaat Formation outcrop sections: AR = Alpha River; MI = Milne Inlet; TS = Tay Sound; WB = White Bay
LS = limestone
DS = dolostone
Standard error = standard deviation (s.d.) of isotopic values divided by the square root of n (number of runs)
% detrital Cr = derived from sample Cr/Al ratios using average shale composition as a proxy for detrital sediment (Cr = 90 ppm; Al = 8.89 wt. %)
$\delta^{53}Cr_{auth}$ = Cr-isotopic composition of the authigenic seawater component corrected for the detrital component
RED = diagenetically-altered carbonate excluded from discussion on Cr-isotopes
BLUE = % detrital Cr > ~35 % so that $\delta^{53}Cr_{auth}$ cannot be calculated

Table S-2 $\delta^{13}C$, $\delta^{18}O$, major and trace element data, as well as sedimentary environments for the Turukhansk Uplift, Vazante and El Mreiti groups, and the Angmaat Formation (~1.1 to 0.9 Ga).

Sample	$\delta^{13}C$ (‰)*	$\delta^{18}O$ (‰)*	Sr (ppm)	Mn (ppm)	Mn/Sr	Fe (ppm)	Ti (ppm)	Zr (ppm)	Depositional environment
TURUKHANSK									
K95-9	-0.1	-9.6	360	481	1.33	5276	10.04	0.31	Near FWWB
K95-22	0.3	-7.5	545	27	0.05	276	-	-	Intertidal to shallow subtidal
K95-76	0.2	-6.4	598	75	0.13	1004	2.39	0.14	Intertidal to shallow subtidal
K95-86	3.2	-7.1	937	27	0.03	85	2.73	0.44	Intertidal to shallow subtidal
K95-88-1	1.2	-7	386	64	0.16	94	2.65	0.12	Intertidal to shallow subtidal
K95-38	2.4	-5.9	145	104	0.72	878	2.76	0.2	Open shelf above FWWB
K95-129-175	-	-	171	258	1.5	1011	3.07	0.4	Below SWB
K95-140-34	-	-	106	412	3.9	4370	2.22	0.3	Below SWB
K95-140-38	1.2	-7.7	125	752	6.04	7323	3.3	0.57	Below SWB
K95-140-43			83	555	6.66	1995	1.26	0.31	Below SWB
K95-140-155	2.3	-7	44	236	5.31	1988	3.25	0.49	Below SWB
K95-140-177	2	-7.2	88	419	4.78	7273	5.12	0.94	Below SWB
K95-142-1	3	-6.3	50	238	4.79	3995	2.96	0.96	Between FWWB and SWB
K95-142-15	-	-	48	197	4.13	1991	2.64	0.65	Between FWWB and SWB
K95-142-20	3	-6.4	45	218	4.81	1851	2.88	0.36	Between FWWB and SWB
K95-142-25	-	-	39	177	4.53	1378	1.92	0.75	Between FWWB and SWB
K95-142-30	3	-6.8	43	173	4.08	1714	3.03	2.01	Between FWWB and SWB
K95-142-60	2.9	-6.5	44	283	6.48	3218	3.84	0.53	Between FWWB and SWB
K95-142-65	2.6	-8.3	32	275	8.47	2706	2.69	0.9	Between FWWB and SWB
K95-140-48	1.7	-7.4	37	3298	88.54	16490	-	-	Below SWB
K95-140-126	0.7	-10.2	141	12144	86.03	20283	-	-	Below SWB
VAZANTE									
KV 500 3	-0.7	-6.9	47	112	2.4	1005	7.1	0.32	Supratidal to intertidal
KV 279 05	1.6	-4.5	61	89	1.45	637	7.6	0.39	Supratidal to intertidal
KV 279 12	-	-	27	103	3.76	815	-	-	Supratidal to intertidal
KV 279 11	-0.6	-7.7	52	413	7.92	1701	4.09	0.37	Supratidal to intertidal
KV 279 01	2.2	-7.7	67	163	2.43	1496	2.96	0.19	Supratidal to intertidal
MAS 1006	-	-	206	2319	11.27	23698	8.51	1.41	Intertidal to shallow subtidal
MAS 1002.5	-	-	159	1473	9.26	16832	10.96	1.49	Intertidal to shallow subtidal
MAS 94	-	-	160	1652	10.35	18649	8.76	0.89	Intertidal to shallow subtidal
MAS 92	0.4	-7.6	64	388	6.06	5877	4.64	0.23	Intertidal to shallow subtidal
MAS 86	-3.4	-8.9	367	1465	4.01	45334	12.38	0.81	Intertidal to shallow subtidal
MAS 83	-3.8	-9	367	1318	3.61	37348	9.24	0.92	Intertidal to shallow subtidal
MAS 82	-2.4	-8.5	249	1689	6.82	53939	17.9	1.35	Intertidal to shallow subtidal
MAS 81	-3.6	-9.1	232	1513	6.54	25869	9.82	1.01	Intertidal to shallow subtidal
MAS 73	-0.3	-5.8	91	567	6.24	10710	8.92	0.52	Intertidal to shallow subtidal
MAS 72	-0.4	-5.7	86	475	5.55	10218	13.54	0.72	Intertidal to shallow subtidal

Sample	$\delta^{13}C$ (‰)*	$\delta^{18}O$ (‰)*	Sr (ppm)	Mn (ppm)	Mn/Sr	Fe (ppm)	Ti (ppm)	Zr (ppm)	Depositional environment
MAS 70	0.7	-6.2	82	477	5.82	8962	9.28	0.5	Intertidal to shallow subtidal
MAS 69	0.5	-6.4	111	490	4.41	9309	9.52	1.09	Intertidal to shallow subtidal
MAS 60	0.7	-7.4	86	429	4.98	11291	10.72	1.93	Intertidal to shallow subtidal
MAS 57	0	-7.2	80	691	8.64	9886	-	-	Intertidal to shallow subtidal
MAS 52	-0.3	-8.8	207	1149	5.57	42787	55.87	1.53	Intertidal to shallow subtidal
MAS 46	0	-8	139	519	3.74	18261	21.21	1.16	Intertidal to shallow subtidal
MAS 38	-0.8	-9.7	204	1421	6.98	36801	44.42	1.53	Intertidal to shallow subtidal
MAS 22	-0.1	-9.3	216	1435	6.65	32330	27.37	1.38	Intertidal to shallow subtidal
MAS 16	0.3	-8.5	229	1070	4.68	27802	12.87	2.16	Intertidal to shallow subtidal
MAS 13	0	-7.7	95	488	5.15	10775	9.31	1.07	Intertidal to shallow subtidal
MAS 08	-1.9	-9.8	232	1874	8.11	24446	10.41	1.45	Intertidal to shallow subtidal
MAS 07	-1.1	-7.8	153	420	2.75	6941	7.28	1.08	Intertidal to shallow subtidal
MAS 06	0.5	-7.1	161	400	2.49	10056	5.08	0.75	Intertidal to shallow subtidal
MAS 04	-0.6	-6.9	82	423	5.14	9992	6.37	0.96	Intertidal to shallow subtidal
MAS 02	-0.8	-7.6	103	708	6.86	17616	7.67	2	Intertidal to shallow subtidal
KV 279 13	3.2	-12.3	28	102	3.7	737	-	-	Supratidal to intertidal
MAS 87	-8.2	-9.4	44	21224	485.1	380558	-	-	Intertidal to shallow subtidal
MAS 80	-5.5	-10.6	306	4928	16.16	101215	-	-	Intertidal to shallow subtidal
MAS 79	-2.1	-8.7	284	4320	15.28	91530	-	-	Intertidal to shallow subtidal
MAS 78	-5.5	-10.9	223	5170	23.23	77272	-	-	Intertidal to shallow subtidal
MAS 77	-2.9	-9.2	150	2796	18.63	42294	-	-	Intertidal to shallow subtidal
MAS 76	-0.3	-5.6	53	1384	26.35	11317	-	-	Intertidal to shallow subtidal
MAS 74	-2.5	-6.9	116	1518	13.1	31889	-	-	Intertidal to shallow subtidal
MAS 30	-1	-11.1	413	672	1.64	12005	-	-	Intertidal to shallow subtidal
MAS 12	-4.3	-10.1	390	1757	4.53	51256	-	-	Intertidal to shallow subtidal
MAS 11	-3.3	-10.8	356	858	2.43	38041	-	-	Intertidal to shallow subtidal
MAS 10	-4.3	-11	475	1510	3.2	49601	-	-	Intertidal to shallow subtidal
MAS 09	-2.5	-10.5	670	2973	4.49	58557	-	-	Intertidal to shallow subtidal
EL MREITI									
F4-48	0.8	-7.5	253	807	3.19	1799	3.18	0.32	Epicratonic near FWWB
F4-80	-5.1	-9	443	2360	5.33	14219	7.97	0.48	Epicratonic above FWWB
F4-87	-5.2	-8.6	467	1613	3.45	11260	2.54	0.5	Epicratonic above FWWB
F4-89	-4.5	-7.5	407	1670	4.1	9479	5.53	0.63	Epicratonic above FWWB
F4-90	-4.6	-9	376	1629	4.34	9323	3.78	0.62	Epicratonic above FWWB
F4-92	-5.4	-8.2	218	2274	10.43	8930	6.34	0.7	Epicratonic above FWWB
F4-95	-4.6	-10.1	165	1372	8.33	7265	5.73	0.59	Epicratonic above FWWB
F4-97	-4.2	-8	130	981	7.53	3717	5.73	0.64	Epicratonic above FWWB
F4-99	-3.7	-7.3	95	694	7.29	927	3.29	0.12	Epicratonic near FWWB
F4-101	-3.4	-7.3	106	483	4.54	667	3.41	0.22	Epicratonic near FWWB
F4-105	-2.7	-6.7	116	351	3.03	1028	3.31	0.13	Epicratonic near FWWB

Sample	$\delta^{13}C$ (‰)*	$\delta^{18}O$ (‰)*	Sr (ppm)	Mn (ppm)	Mn/Sr	Fe (ppm)	Ti (ppm)	Zr (ppm)	Depositional environment
F4-107	-2.7	-7.5	123	336	2.74	1310	2.6	0.28	Epicratonic near FWWB
F4-109	-2.3	-7.3	145	435	3	5453	3.7	0.41	Epicratonic near FWWB
F4-111	-2.2	-7.3	184	309	1.68	3032	3.67	0.5	Epicratonic near FWWB
F4-113	-2	-7.7	309	290	0.94	1887	3.71	0.3	Epicratonic near FWWB
F4-115	-1.1	-7	155	163	1.05	732	3.52	0.1	Epicratonic near FWWB
F4-19	-2.3	-5.7	97	1499	15.53	6024	-	-	Epicratonic intertidal to shallow subtidal
F4-21	-2.9	-4.2	97	2498	25.81	26646	-	-	Epicratonic intertidal to shallow subtidal
ANGMAAT									
A2-37855	2.3	-3.9	52	200	3.85	1100	7.74	0.15	Subtidal
MI-27390	-	-	35	109	3.09	106	5.45	0.07	Shallow subtidal ooid shoal
MI-27450	-	-	38	110	2.9	132	5.65	0.03	Shallow subtidal ooid shoal
MI-3420	-	-	37	77	2.1	90	4.3	0.05	Shallow subtidal ooid shoal
TY-13	-	-	53	223	4.21	351	4.59	0.08	Supratidal to intertidal
TY-18025B	3.1	-3.5	52	280	5.39	460	5.28	0.06	Supratidal to intertidal
TP-24260	-	-	41	72	1.74	195	7.01	0.28	Supratidal to intertidal
TY-3975	-	-	59	311	5.24	494	4.96	0.03	Supratidal to intertidal
TY-4	-	-	54	196	3.61	275	9.99	0.25	Supratidal to intertidal
WB-13284A	-	-	65	315	4.81	582	3.92	0.11	Intertidal to shallow subtidal
WB-3600	-	-	65	275	4.21	333	6.84	0.05	Intertidal to shallow subtidal
WB-815	-	-	63	107	1.71	294	7.19	0.37	Intertidal to shallow subtidal
WB2-7955	-	-	35	125	3.56	229	4.29	0.06	Intertidal to shallow subtidal
WB2-8765	1.7	-2.7	68	183	2.7	277	8	0.08	Intertidal to shallow subtidal
WB94-12	2.6	-2.5	41	299	7.23	520	5.65	0.08	Intertidal to shallow subtidal
WB94-14	2.7	-0.7	44	364	8.2	597	6.22	0.1	Intertidal to shallow subtidal
WB94-3	3.3	-2.4	58	97	1.66	231	5.81	0.04	Intertidal to shallow subtidal
WB94-6	3	-4	46	240	5.19	470	3.75	0.03	Intertidal to shallow subtidal
WB94-16	2.9	-2.8	68	702	10.33	1483	8.48	0.11	Intertidal to shallow subtidal

*$\delta^{13}C$ and $\delta^{18}O$ data previously published for the Turukhansk Uplift (Bartley *et al.*, 2001), Vazante Group (Azmy *et al.*, 2001), El Mreiti Group (Gilleaudeau and Kah, 2013a), and Angmaat Formation (Kah *et al.*, 1999).
FWWB = fair weather wave base; SWB = storm wave base
RED = diagenetically-altered carbonate excluded from discussion on Cr-isotopes
BLUE = % detrital Cr > ~35 % so that $\delta^{53}Cr_{auth}$ cannot be calculated

Supplementary Information References

Azmy, K., Veizer, J., Misi, A., de Oliveira, T.F., Sanches, A.L., Dardenne, M.A. (2001) Dolomitization and isotope stratigraphy of the Vazante Formation, São Francisco Basin, Brazil. *Precambrian Research* 112, 303-329.

Azmy, K., Kendall, B., Creaser, R.A., Heaman, L., de Oliveira, T.F. (2008) Global correlation of the Vazante Group, São Francisco Basin, Brazil: Re-Os and U-Pb radiometric age constraints. *Precambrian Research* 164, 160-172.

Azmy, K., Sylvester, P., de Oliveira, T.F. (2009) Oceanic redox conditions in the Late Mesoproterozoic recorded in the upper Vazante Group carbonates of the São Francisco Basin, Brazil: evidence from stable isotopes and REEs. *Precambrian Research* 168, 259-270.

Banner, J.L., Hanson, G.N. (1990) Calculation of simultaneous isotopic and trace element variations during water-rock interaction with applications to carbonate diagenesis. *Geochimica et Cosmochimica Acta* 54, 3123-3137.

Bartley, J.K., Semikhatov, M.A., Kaufman, A.J., Knoll, A.H., Pope, M.C., Jacobsen, S.B. (2001) Global events across the Mesoproterozoic-Neoproterozoic boundary: C and Sr isotopic evidence from Siberia. *Precambrian Research* 111, 165-202.

Bartley, J.K., Kah, L.C., McWilliams, J.L., Stagner, A.F. (2007) Carbon isotope chemostratigraphy of the Middle Riphean type section (Avzyan Formation, Southern Urals, Russia): signal recovery in a fold-and-thrust belt. *Chemical Geology* 237, 211-232.

Benan, C.A.A., Deynoux, M. (1998) Facies analysis and sequence stratigraphy of Neoproterozoic platform deposits in Adrar of Mauritania, Taoudeni Basin, West Africa. *Geologische Rundschau* 87, 283-330.

Bertrand-Sarfati, J., Moussine-Pouchkine, A. (1988) Is cratonic sedimentation consistent with available models? An example from the Upper Proterozoic of the West African craton. *Sedimentary Geology* 58, 255-276.

Dorobek, S.L. (1987) Petrography, geochemistry, and origin of burial diagenetic facies, Siluro-Devonian Helderberg Group (carbonate rocks), central Appalachians. *AAPG Bulletin* 71, 492-514.

Frei, R., Gaucher, C., Døssing, L.N., Sial, A.N. (2011) Chromium isotopes in carbonates – a tracer for climate change and for reconstructing the redox state of ancient seawater. *Earth and Planetary Science Letters* 312, 114-125.

Geboy, N.J., Kaufman, A.J., Walker, R.J., Misi, A., de Oliveira, T.F., Miller, K.E., Azmy, K., Kendall, B., Poulton, S.W. (2013) Re-Os constraints and new observations of Proterozoic glacial deposits in the Vazante Group, Brazil. *Precambrian Research* 238, 199-213.

Gilleaudeau, G.J., Kah, L.C. (2013a) Carbon isotope records in a Mesoproterozoic epicratonic sea: carbon cycling in a low-oxygen world. *Precambrian Research* 228, 85-101.

Gilleaudeau, G.J., Kah, L.C. (2013b) Oceanic molybdenum drawdown by epeiric sea expansion in the Mesoproterozoic. *Chemical Geology* 356, 21-37.

Gilleaudeau, G.J., Kah, L.C. (2015) Heterogeneous redox conditions and a shallow chemocline in the Mesoproterozoic ocean: evidence from carbon-sulfur-iron relationships. *Precambrian Research* 257, 94-108.

Heaman, L.M., LeCheminant, A.N., Rainbird, R.H. (1992) Nature and timing of Franklin igneous events, Canada: implications for a late Proterozoic mantle plume and the break-up of Laurentia. *Earth and Planetary Science Letters* 109, 117-131.

Kah, L.C., Sherman, A.B., Narbonne, G.M., Kaufman, A.J., Knoll, A.H. (1999) $\delta^{13}C$ stratigraphy of the Proterozoic Bylot Supergroup, northern Baffin Island: implications for regional lithostratigraphic correlations. *Canadian Journal of Earth Sciences* 36, 313-332.

Kah, L.C., Lyons, T.W., Chesley, J.T. (2001) Geochemistry of a 1.2 Ga carbonate-evaporite succession, northern Baffin and Bylot Islands: implications for Mesoproterozoic marine evolution. *Precambrian Research* 111, 203-234.

Kah, L.C., Bartley, J.K., Teal, D.A. (2012) Chemostratigraphy of the late Mesoproterozoic Atar Group, Taoudeni Basin, Mauritania: muted isotopic variability, facies correlation, and global isotopic trends. *Precambrian Research* 200-203, 82-103.

Kaufman, A.J., Knoll, A.H. (1995) Neoproterozoic variations in the C-isotopic composition of seawater: stratigraphic and biogeochemical implications. *Precambrian Research* 73, 27-49.

Knoll, A.H., Kaufman, A.J., Semikhatov, M.A. (1995) The carbon-isotopic composition of Proterozoic carbonates: Riphean successions from northwestern Siberia (Anabar Massif, Turukhansk Uplift). *American Journal of Science* 295, 823-850.

Longman, M.W. (1980) Carbonate diagenetic textures from near surface diagenetic environments. *AAPG Bulletin* 64, 461-487.

Mazzullo, S.J. (1992) Geochemical and neomorphic alteration of dolomite: a review. *Carbonates and Evaporites* 7, 21-37.

Nicholas, C.J. (1996) The Sr isotopic evolution of the oceans during the 'Cambrian Explosion'. *Journal of the Geological Society of London* 153, 243-254.

Olcott, A.N., Sessions, A.L., Corsetti, F.A., Kaufman, A.J., de Oliveira, T.F. (2005) Biomarker evidence for photosynthesis during Neoproterozoic glaciation. *Science* 310, 471-474.

Ovchinnikova, G.V., Gorokhov, I.M., Belyatskii, B.V. (1995) U-Pb systematics of Pre-Cambrian carbonates: the Riphean Sukhaya Tunguska Formation in the Turukhansk Uplift, Siberia. *Lithology and Mineral Resources* 30, 525–536.

Petrov, P.Y. (1993a) Depositional environments of the lower formations of the Riphean sequence, northern part of the Turukhansk Uplift, Siberia. *Stratigraphy and Geological Correlation* 1, 181-191.

Petrov, P.Y. (1993b) Structure and sedimentation environments of the Riphean Bezymyannyi Formation in the Turukhansk Uplift, Siberia. *Stratigraphy and Geological Correlation* 1, 490-502.

Petrov, P.Y., Semikhatov, M.A. (1997) Structure and environmental conditions of a transgressive Upper Riphean complex: Miroyedikha Formation of the Turukhansk Uplift, Siberia. *Lithology and Mineral Resources* 32, 11-29.

Petrov, P.Y., Semikhatov, M.A. (1998) The upper Riphean stromatolitic reefal complex; Burovaya Formation of the Turukhansk region, Siberia. *Lithology and Mineral Resources* 33, 539-560.

Petrov, P.Y., Semikhatov, M.A., Sergeev, V.N. (1995) Development of the Riphean carbonate platform and distribution of silicified microfossils: the Sukhaya Tunguska Formation, Turukhansk Uplift, Siberia. *Stratigraphy and Geological Correlation* 3, 602-620.

Reid, R.P., Macintyre, I.G. (1998) Carbonate recrystallization in shallow marine environments: a widespread diagenetic process forming micritized grains. *Journal of Sedimentary Research* 68, 928-946.

Rooney, A.D., Selby, D., Houzay, J.P., Renne, P.R. (2010) Re – Os geochronology of a Mesoproterozoic sedimentary succession, Taoudeni Basin, Mauritania: implications for basin-wide correlations and Re – Os organic-rich sediments systematics. *Earth and Planetary Science Letters* 289, 486-496.

Schoenberg, S., Zink, M., Staubwasser, M., von Blanckenburg, F. (2008) The stable Cr isotope inventory of solid Earth reservoirs determine by double spike MC-ICP-MS. *Chemical Geology* 249, 294-306.

Sergeev, V.N. (2001) Paleobiology of the Neoproterozoic (Upper Riphean) Shorikha and Burovaya silicified microbiotas, Turukhansk Uplift, Siberia. *Journal of Paleontology* 75, 427-448.

Sergeev, V.N., Knoll, A.H., Petrov, P.Y. (1997) Paleobiology of the Mesoproterozoic-Neoproterozoic transition: the Sukhaya Tunguska Formation, Turukhansk Uplift, Siberia. *Precambrian Research* 85, 201-239.

Scheiderich, K., Amini, M., Holmden, C., Francois, R. (2015) Global variability of chromium isotopes in seawater demonstrated by Pacific, Atlantic, and Arctic Ocean samples. *Earth and Planetary Science Letters* 423, 87-97.

Taylor, S.R., McLennan, S.M. (1985) The continental crust: its composition and evolution. Blackwell Scientific Publications, Palo Alto, CA, 312 pp.

Tucker, M.E. (1983) Diagenesis, geochemistry, and origin of a Precambrian dolomite: the Beck Spring Dolomite of eastern California. *Journal of Sedimentary Petrology* 53, 1097-1119.

TURNER, E.C., KAMBER, B.S. (2012) Arctic Bay Formation, Borden Basin, Nunavut (Canada): Basin evolution, black shale, and dissolved metal systematics in the Mesoproterozoic ocean. *Precambrian Research* 208-211, 1-18.

ULLMANN, C.V., KORTE, C. (2015) Diagenetic alteration in low-Mg calcite from macrofossils: a review. *Geological Quarterly* 59, 3-20.

VAHRENKAMP, V.C., SWART, P.K. (1990) New distribution coefficient for the incorporation of strontium into dolomite and its implications for the formation of ancient dolomites. *Geology* 18, 387-391.

VEIS, A.F., PETROV, P.Y. (1994) The main peculiarities of the environmental distribution of microfossils in the Riphean basins of Siberia. *Stratigrarphy and Geological Correlation* 2, 97-129.

WEDEPOHL, K.H. (1991) The composition of the upper Earth's crust and the natural cycles of selected metals. In: Merian, E. (Ed.) *Metals and their compounds in the environment: occurrence, analysis, and biological relevance*. VCH, Weinheim, New York, Basel, Cambridge, 3-17.